Science of the Total Environment 762 (2021) 143100

Contents lists available at ScienceDirect

Science of the Total Environment

journal homepage: www.elsevier.com/locate/scitotenv

Activation properties of aerosol particles as cloud condensation nuclei at urban and high-altitude remote sites in southern Europe

Fernando Rejano [a,b,*], Gloria Titos [a,b], Juan Andrés Casquero-Vera [a,b], Hassan Lyamani [a,b], Elisabeth Andrews [c], Patrick Sheridan [c], Alberto Cazorla [a,b], Sonia Castillo [a,b], Lucas Alados-Arboledas [a,b], Francisco José Olmo [a,b]

[a] Andalusian Institute for Earth System Research, IISTA-CEAMA, University of Granada, Junta de Andalucía, Granada 18006, Spain
[b] Department of Applied Physics, University of Granada, Granada 18071, Spain
[c] Earth System Research Laboratory, National Oceanic and Atmospheric Administration, Boulder, CO, 80305, United States

HIGHLIGHTS

- A joint analysis of CCN properties were performed at two different sites.
- CN and CCN concentrations are driven by anthropogenic emissions at the urban site.
- At the mountain site, CCN are influenced by upslope transport of pollutants.
- NPF events are an important source of CCN at the mountain site during summer.
- Two empirical models were used to estimate CCN from ancillary measurements.

GRAPHICAL ABSTRACT

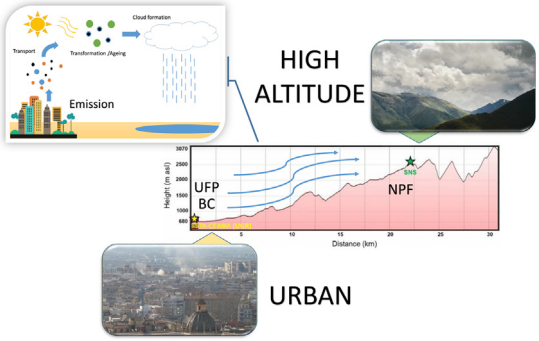

ARTICLE INFO

Article history:
Received 30 July 2020
Received in revised form 8 October 2020
Accepted 13 October 2020
Available online 16 October 2020

Editor: Pavlos Kassomenos

Keywords:
Cloud condensation nuclei
New particle formation
High-altitude remote site empirical model

ABSTRACT

Understanding the activation properties of aerosol particles as cloud condensation nuclei (CCN) is important for the climate and hydrological cycle, but their properties are not fully understood. In this study, the CCN activation properties of aerosols are investigated at two different sites in southern Spain: an urban background station in Granada and a high altitude mountain station in the Sierra Nevada National Park, with a horizontal separation of 21 km and vertical separation of 1820 m.

CCN activity at the urban environment is driven by primary sources, mainly road traffic. Maximum CCN concentrations occurred during traffic rush hours, although this is also when the activation fraction is lowest. This is due to the characteristics of the rush hour aerosol consisting of ultrafine and less hygroscopic particles. In contrast, the mountain site exhibited larger and more hygroscopic particles, with CCN activity driven by the joint effect of new particle formation (NPF) and vertical transport of anthropogenic particles from Granada urban area by orographic buoyant upward flow. This led to the maximum concentrations of CCN and aerosol particles occurring at midday at the mountain site. Clear differences in the diurnal evolution of CCN between NPF events and non-event days were observed at the Sierra Nevada station, demonstrating the large contribution of NPF to CCN concentrations, especially at high supersaturations. The isolated contribution of NPF to CCN concentration has been estimated to be 175% higher at $SS = 0.5\%$ relative to what it would be without NPF. We conclude that NPF could be the major source of CCN at this mountain site.

* Corresponding author at: Andalusian Institute for Earth System Research, IISTA-CEAMA, University of Granada, Junta de Andalucía, Granada 18006, Spain.
E-mail address: frejano@ugr.es (F. Rejano).

https://doi.org/10.1016/j.scitotenv.2020.143100

Finally, two empirical models were used to parameterize CCN concentration in terms of aerosol optical or physical parameters. The models can explain measurements satisfactorily at the urban station. At the mountain site both models cannot reproduce satisfactorily the observations at low *SS*.

1. Introduction

Cloud droplets are formed by the activation of a subset of aerosol particles called cloud condensation nuclei (CCN). Changes in the amount or in the CCN properties will result in changes in cloud properties, potentially affecting precipitation and the radiative impact of clouds (Lohmann and Feichter, 2005). In this sense, the concentration of CCN is an essential parameter affecting aerosol–cloud interactions, ACI. The radiative forcing associated with the indirect effect of aerosols through ACI (-0.55 ± 0.63 Wm^{-2}) is larger than the direct effect of aerosol through aerosol–radiation interaction (-0.27 ± 0.50 Wm^{-2}) (Intergovernmental Panel on Climate Change, 2014). In addition, the uncertainty associated with the indirect aerosol forcing remains high and is significantly larger than that associated with the direct aerosol forcing (Intergovernmental Panel on Climate Change, 2014). Despite the considerable efforts aimed at better understanding ACI during the last few years, the uncertainty associated with the radiative forcing due to ACI has not decreased significantly (Seinfeld et al., 2016). Reducing this uncertainty is crucial for increasing our confidence in predictions of global and regional climate models (Intergovernmental Panel on Climate Change, 2014). One of the leading causes of this uncertainty is a lack of broad knowledge about particle sources and how particles evolve to become effective CCN (Fanourgakis et al., 2019). Thus, the quantification of CCN concentrations, their spatial variability, the identification of their sources and the characterization of the relevant aerosol properties involved in the activation process of aerosol particles as CCN are critical aspects to reduce this uncertainty (Crosbie et al., 2015; Paramonov et al., 2015; Schmale et al., 2018).

The ability of aerosol particles to act as CCN at a certain supersaturation (*SS*) depends on the particle size and chemical composition (e.g., Seinfeld and Pandis, 1998). CCN are particles that are either directly emitted (i.e., primary particles) into the atmosphere from both anthropogenic (Duan et al., 2018) and natural sources (Després et al., 2012) or aerosol particles that have undergone growth processes and possibly chemical transformations in the atmosphere. These smaller particles may originate from atmospheric new particle formation (NPF), anthropogenic combustion or other emission sources (Chen et al., 2019; Paasonen et al., 2018).

In addition to primary particles, regional NPF events have been identified as an important mechanism producing CCN (Merikanto et al., 2009). The total particle number concentration in regional background conditions, as well as in the global troposphere, is very likely to be dominated by NPF (O'Dowd et al., 2002). Several studies have investigated the impact of NPF on CCN (Dameto de España et al., 2017; Gordon et al., 2017; Kalkavouras et al., 2019; Kerminen et al., 2012; Leng et al., 2014; Rose et al., 2017). According to Merikanto et al. (2009), 45% of global low-level cloud CCN originates from NPF, and 35% of the remaining CCN are formed in the free and upper troposphere. Gordon et al. (2017) pointed out that NPF produces around 50% of CCN at low supersaturations. However, the contribution of NPF to CCN concentration is highly dependent on the environment where it takes place, since NPF variability and intensity varies strongly from one environment to another (Kerminen et al., 2018). At urban sites, NPF can enhance the CCN population between 20 and 40% at low or medium *SS* values (Dameto de España et al., 2017; Leng et al., 2014). However, at remote sites (e.g., mountain stations) NPF can be the major CCN source, increasing the CCN concentration up to 250% (Rose et al., 2017).

Urban areas are important sources of aerosol particles, especially of ultrafine particles (particles with diameter < 100 m) due to the great variety of emission sources. Because of this, high CCN concentrations have been observed in urban areas (Burkart et al., 2011; Che et al., 2016; Ren et al., 2018; Zhang et al., 2017) despite the fact that aerosol particles in urban areas are usually less hygroscopic (Burgos et al., 2019; Titos et al., 2014a). However, although the concentration of particles able to act as CCN is high in urban areas, the CCN activation efficiency is lower than in less polluted environments (Cheung et al., 2020; Cubison et al., 2008; Kim et al., 2014; Schmale et al., 2018). While the highest CCN concentrations are observed in urban environments, mountain sites are also important for the investigation of CCN properties since they are located at the height where atmospheric conditions favor the formation of clouds. Mountain sites are often located in the free troposphere, however, in some circumstances the high altitude sites can be influenced by polluted air injected from lower altitudes. For example, Asmi et al. (2012) have reported the important impact of anthropogenic emissions from Clermont-Ferrand town on CCN properties measured at Puy de Dôme Mountain. Therefore, to have a broad knowledge of CCN properties, research is needed in both urban environments and at mountain sites that can be at times under the influence of urban emissions during specific circumstances.

Unfortunately, CCN measurements are carried out at relatively few sites, in contrast to aerosol physical and optical properties, such as particle number size distribution and aerosol scattering and absorption coefficients, that are routinely measured at many locations around the world within international measurement networks such as NFAN (NOAA Federated Aerosol Network) (Andrews et al., 2019) or ACTRIS (Aerosols, Clouds, Trace gases Research Infrastructure) (Laj et al., 2020; Wiedensohler et al., 2012). Thus, developing empirical models that use these more commonly measured aerosol properties as proxies of N_{CCN} could contribute to improve our understanding of the spatial and temporal variability of CCN data and, hence, reduce indirect aerosol forcing uncertainty. To evaluate this, collocated measurements of CCN and aerosol properties at different sites with distinct aerosol properties and different atmospheric conditions may be of great use in improving parameterizations of CCN.

Different approaches have been proposed for the parameterizations of CCN activity based on aerosol optical properties (e.g., Jefferson, 2010; Shen et al., 2019). Jefferson (2010) showed that using aerosol optical properties as proxies to estimate N_{CCN} provided satisfactory results at several remote sites. This empirical model was able to estimate the measured CCN concentration within $\pm 50\%$ at higher concentrations, while at low CCN concentrations the model overestimated CCN concentrations (Jefferson, 2010). The parameterizations showing the best agreement between predictions and measurements (ratios between 0.95 and 1.05) use aerosol parameters directly related to particle activation as CCN, such as aerosol size distribution, size-resolved chemical composition and mixing state (Che et al., 2017; Ervens et al., 2010; Ren et al., 2018; Zhang et al., 2020). However, these aerosol properties are not routinely available at many sampling sites relative to the availability of optical properties, which limit the application and usefulness of these CCN parameterizations.

Most CCN studies are carried out for short time periods during specific measurement campaigns with special conditions, such as fog events (Hammer et al., 2014; Motos et al., 2019), Saharan dust episodes (Weger et al., 2018), biomass burning events (Bougiatioti et al., 2016; Chen et al., 2019; Wu et al., 2017) or polluted conditions (Duan et al., 2018), among others. Other studies are focused on long-term data sets from a specific experimental site (Crosbie et al., 2015; Burkart et al., 2011; Jurányi et al., 2011; Dameto de España et al., 2017). Alternatively,

some studies provide an overview of CCN measurements at different sampling sites around the world in order to characterize the spatial variability of CCN activity (Paramonov et al., 2015; Schmale et al., 2018). To date, studies that perform a joint analysis of CCN from multiple, interconnected sampling sites and investigate how they are related are scarce (Zhang et al., 2017).

In this study, the combined analysis of CCN concentrations, aerosol size distributions and aerosol optical property measurements at two experimental stations located in very different environments in south-eastern Spain is presented. The two sites are an urban background station located in the city of Granada (680 m a.s.l.) and an alpine station located in Sierra Nevada mountain range, at 2500 m a.s.l., 21 km south-east of Granada. We first characterize the activation properties of aerosol particles at these two sites, and assess the impact of local pollution from the Granada urban area on the Sierra Nevada aerosol activation properties. We then estimate the contribution of NPF events to CCN concentration at the Sierra Nevada station. Finally, we test the predictions of CCN concentration using two different empirical models to develop a simple parameterization of CCN activity at each site.

2. Measurements and instrumentation

2.1. Experimental sites

The study was carried out in south-eastern Spain, and the measurements were performed at AGORA observatory (Andalusian Global Observatory of the Atmosphere). AGORA includes two completely different experimental stations: an urban background station located in the city of Granada (37.18°N, 3.58°W, 680 m a.s.l., UGR), at the Andalusian Institute for Earth System Research (IISTA-CEAMA), and an alpine station located in Sierra Nevada mountain range at the Albergue Universitario (37.10° N, 3.39° W, 2500 m a.s.l., SNS). The stations are separated horizontally by a distance of 21 km and the difference in height is approximately 1820 m. Both stations are situated in the central European time zone (i.e., local time is UTC $\pm$ 1 h and UTC $\pm$ 2 h during the daylight saving time period). These stations are part of ACTRIS (Aerosol, Cloud and Trace gases Research Infrastructure, http://actris.eu) (Pandolfi et al., 2018) and are included in the NOAA Federated Aerosol Network, NFAN (Andrews et al., 2019). While local sources impacting each site are described below, the two major external aerosol sources affecting the study area are anthropogenic pollution from the European continent and Saharan dust from North Africa (Lyamani et al., 2005; Valenzuela et al., 2012).

Granada is a medium-size city with a population of 232.208 (www.ine.es, 2018), which increases up to 530.000 if the whole metropolitan area is considered. The city is situated in a natural basin surrounded by mountains with summit elevations between 1000 and 3400 m a.s.l. Granada is a non-industrialized city and one of the Spanish cities that suffers from pollution problems (Casquero-Vera et al., 2019) The main local aerosol source is road traffic, including both motor vehicle exhaust and re-suspension of particulate material from the roadways (Titos et al., 2014b). In winter, domestic heating and biomass burning for agricultural waste removal are additional sources of anthropogenic pollution (Lyamani et al., 2010; Titos et al., 2017). Moreover, the orography of Granada favors winter temperature inversions and predominance of very weak wind speeds, which can lead to a large accumulation of particles near the surface (Lyamani et al., 2012) and may cause environmental and human health problems.

Sierra Nevada exhibits wide climatic diversity, with big thermal oscillations due to the altitudinal breadth, latitude and the complex topography of the terrain. The alpine measurement station experiences strong insolation, with relatively arid conditions, due to the west-east orientation of the mountain range. Due to its high altitude, the aerosol particles over SNS station are often representative of the pristine free troposphere conditions, especially in winter and night time. During summer, SNS station is frequently influenced by transport of pollutants from Granada city to Sierra Nevada station as a result of mixing layer growth and the activation of the mountain-valley breeze phenomenon as well as NPF events at midday (De Arruda Moreira et al., 2019; Casquero-Vera et al., 2020).

2.2. Aerosol sampling and instrumentation

Air sampling for all instruments was obtained from the top of a stainless steel tube, 20 cm diameter and 5 m length at UGR (Lyamani et al., 2008), and 10 cm in diameter and 2.5 m in length at SNS (Bedoya-Velásquez et al., 2018). At both stations, inside the stainless steel tube there are several stainless steel pipes, which provide sample air to the different instruments. All measurements reported here refer to ambient conditions and were performed without aerosol size cut. The instruments used in this study are briefly described below and data coverage of the instruments is shown in Fig. 1. The measurement campaign at UGR was from October 2018 to May 2019, while at SNS station the measurement campaign covers the summer season (from June to August of 2019).

2.2.1. CCN measurements

In order to measure polydisperse CCN number concentrations at different supersaturations (*SS*), a Continuous-Flow Streamwise Thermal-Gradient CCN chamber (DMT, model CCN-100) (Roberts and Nenes,

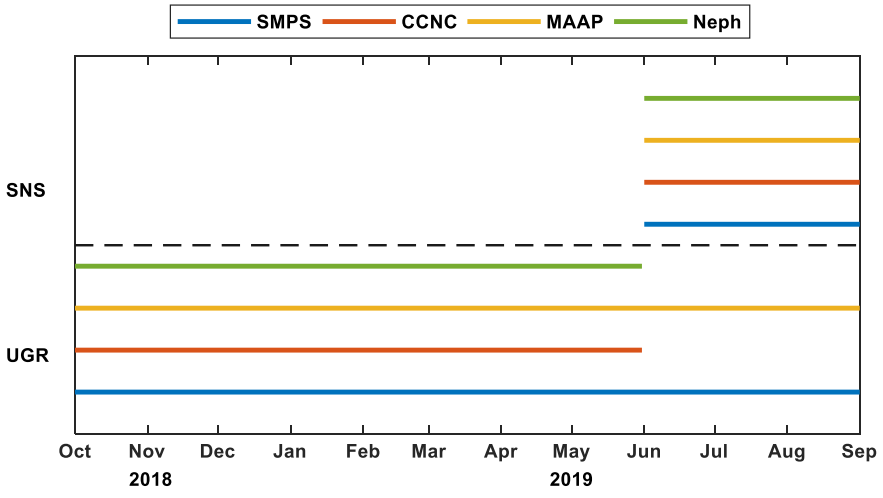

Fig. 1. Data coverage of the instruments used in this study for the studied period from October of 2018 to August of 2019.

2005) was connected to the inlet with a total flow rate of 0.5 lpm and 9:1 sheath-to-sample flow ratio. The CCN counter (CCNC) was calibrated at the beginning and at the end of the measurement period following the ACTRIS guidelines (available in http://actris.nilu.no/Content/SOP) and performing *SS* scans. Both calibrations provided satisfactory results and showed little deviation in the calibration from the beginning to the end of the campaign. The main *SS* values used in this study were 0.2, 0.3, 0.4, 0.5, 0.6 and 0.9% at the urban site and 0.17, 0.25, 0.30, 0.40, 0.50 and 0.7% at the high-altitude site. A complete cycle covering the whole *SS* spectrum lasted 1 h, taking 10 min at each *SS* value. The temporal resolution of the CCN measurements was 1 min. To guarantee the data quality we follow the ACTRIS standardized protocol for CCN measurements and data processing (available in http://actris.nilu.no/Content/SOP). Following this protocol, the CCN data have been filtered as follows. In the first step, only data with *SS* above the 1st percentile and below the 99th percentile have been taken into account for each *SS* setpoint value. Then for each *SS* value, we compute the mean and the standard deviation (STD). Secondly, data above and below 1.5 times the STD are flagged as invalid and are not further used for the study. Normally the first and last points in each *SS* step are the points that do not satisfy the criteria because the supersaturation conditions in the growth chamber are not yet stable.

2.2.2. Aerosol size distribution measurements

Sub-micron aerosol size distribution in the mobility diameter range 10–514 nm were measured with 5-min temporal resolution by a Scanning Mobility Particle Sizer (SMPS, TSI 3938) composed of an electrostatic classifier (TSI 3082) and a Condensation Particle Counter (CPC; TSI 3772) using aerosol and sheath flow rates of 1.0 and 5.0 lpm, respectively. Total aerosol concentration in the SMPS size range (referred here as N_{CN}) was inferred by integrating the aerosol number size distribution. The quality of the SMPS measurements was assured by frequently checking the flow rates, performing 203 nm PSL calibration and with in-situ intercomparison (ACTRIS Round Robin Tour), following the ACTRIS and GAW recommendations (Wiedensohler et al., 2012).

From the size distribution measurements, it is possible to calculate the geometric diameter. It is the diameter below which half of the total aerosol concentration is found and is used as a proxy of aerosol size. It can be obtained from the SMPS measurements from its mathematic definition as follows:

$$0.5 \cdot N_{CN} = \int_{D_{min}}^{D_{geo}} \frac{dN}{dlogD} \quad (1)$$

In our case the D_{min} is the lower limit of the SMPS which is 10 nm.

2.2.3. Aerosol optical measurements

Aerosol light scattering (σ_{sp}) and backscattering coefficients (σ_{bsp}) were measured with an integrating nephelometer (TSI, model 3563) at three wavelengths 450, 550 and 700 nm. The nephelometer operated at a flow rate of 15 lpm. The correction proposed by Anderson and Ogren (1998) has been applied to account for the angular truncation and non-idealities of the light source (deviations from a Lambertian distribution of light). Nephelometer data was collected with a time resolution of 1 min.

The absorption coefficient of particles (σ_{ap}) at 637 nm was measured using a Multi-Angle Absorption Photometer (MAAP, Thermo Scientific model 5012). This instrument is the most reliable filter-based instrument for aerosol absorption coefficient measurements (Petzold and Schönlinner, 2004). The MAAP uses a constant flow rate of 16.7 lpm and provides 1-minute values. Black Carbon (BC) concentration was obtained from MAAP measurements by dividing the measured σ_{ap}(637 nm) by the mass absorption cross section of 6.6 $m^2\ g^{-1}$ (Müller et al., 2011).

Several optical parameters, which provide information related to aerosol size and composition, have been inferred from the aforementioned aerosol optical property measurements. The Backscatter Fraction (BSF) is defined as the ratio between the backscattering (σ_{bsp}) and scattering (σ_{sp}) coefficients at the same wavelength (450 nm in this study):

$$BSF = \frac{\sigma_{bsp}}{\sigma_{sp}} \quad (2)$$

This parameter acts as a proxy of the predominant particles' size in the aerosol population (i.e. higher values of BSF are related to a predominance of smaller particles). The scattering Ångström exponent (SAE), which characterizes the wavelength dependence of σ_{sp}, is another proxy for the particle mean size. It was calculated according to the following equation for $\lambda_1 = 550$ and $\lambda_2 = 700$ nm:

$$SAE_{550-700} = \frac{\log \sigma_{sp}(\lambda 1) - \log \sigma_{sp}(\lambda 2)}{\log(\lambda 2) - \log(\lambda 1)} \quad (3)$$

SAE takes values around 2 when the scattering process is dominated by fine particles, while it is close to 0 when the scattering process is dominated by coarse particles (Seinfeld and Pandis, 1998). BSF and SAE are sensitive to different parts of the aerosol size distribution (Collaud Coen et al., 2007); BSF is more sensitive to particles in the lower part of the accumulation mode while SAE responds to the upper part of the accumulation mode and the coarse mode. Finally, the single scattering albedo (SSA) is defined as the ratio between the scattering and extinction ($\sigma_{ep} = \sigma_{sp} + \sigma_{ap}$) coefficients and provides information about the predominance of scattering or absorbing particles, which in turn is related to the composition of the particles. The scattering coefficient at 637 nm was calculated using the $SAE_{550-700}$ according to Ångström's law in order to estimate the SSA at the same wavelength as the absorption measurement.

3. Data analysis and determination of activation parameters

In this section, we present a brief overview of the fundamentals of κ-Köhler theory and the methodology used to calculate the critical diameter and the κ parameter. We then present the procedure followed to estimate the concentration of CCN from other aerosol properties such as aerosol optical properties or size distribution parameters.

3.1. κ-Köhler theory

The activation of a particle to a cloud droplet at a given *SS* depends on its dry diameter (D_{dry}) and chemical composition. Classical Köhler theory (Köhler, 1936) describes the equilibrium saturation ratio (*S*; *S = SS-1*) over a solution droplet in terms of its diameter. The Köhler model takes into account the Kelvin curvature effect, related to particle size, and the Raoult effect, capturing the influence of particle chemical composition. This theory is applied to an individual droplet. In order to simplify the Raoult effect, Petters and Kreidenweis (2007) proposed the use of a single hygroscopicity parameter κ to describe the dependence of water activity on solution concentration for a given chemical composition. For atmospheric aerosols, the values of the hygroscopicity parameter range from 0 in the case of non-hygroscopic particles to up to 1.3 in the case of hygroscopic salts. Joining both approaches resulted in the κ-Köhler model, which expresses the equilibrium saturation as a function of the droplet diameter, *D*:

$$S = \frac{D^3 - D_{dry}^3}{D^3 - (1-\kappa)D_{dry}^3} \exp\left(\frac{4\sigma_{s/a}M_w}{RT\rho_w D}\right) \quad (4)$$

where ρ^w and M^w are the density and the molar mass of water, respectively; *R* is the universal gas constant, *T* is the absolute temperature and $\sigma^{s/a}$ is the surface tension of the solution-air interface (assumed to be equal to the surface tension of pure water).

Eq. (4) represents the equilibrium curve of $SS(D)$ for a particle with a given dry diameter and hygroscopicity parameter. This curve has a global maximum and the maximum SS value is called the critical supersaturation (SS_{crit}). Therefore, Eq. (4) provides a relationship between dry diameter of the particle, the hygroscopicity parameter and the critical supersaturation. Note that D_{crit} is defined for a specific particle with known dry size and chemical composition at a certain SS value. In the following section the method used for determining the critical diameter and hygroscopicity parameter in the case of polydisperse aerosol is explained.

3.2. Calculation of the critical diameter D_{crit} and the hygroscopicity parameter κ

In the case of polydisperse measurements, an effective D_{crit} can be calculated by considering both the measured particle number size distribution and the CCN measurements at a fixed SS value and assuming a sharp activation cut-off, which is associated with internally mixed aerosol (Jurányi et al., 2011):

$$N_{CCN}(SS) = \int_{D_{crit}(SS)}^{D_{max}} \frac{dN}{d\log D} d\log D \quad (5)$$

The particle number size distribution is integrated from its upper limit to the diameter at which the integral value equals the simultaneously measured $N_{CCN}(SS)$.

The hygroscopicity parameter is specific for each particle and is related to its chemical composition. However, it is very common and useful to associate an effective value of the hygroscopicity parameter with the whole population of aerosol particles of a specific environment. In order to estimate κ of a particle mixture with different chemical composition, Petters and Kreidenweis (2007) proposed a simple mixing rule in terms of the hygroscopicity parameter of each species and their corresponding volume fraction. This approximation gives a successful explanation of observations (Bougiatioti et al., 2009, 2016; Rose et al., 2010; Wang et al., 2010). Unfortunately, chemical composition measurements are not always available, especially with high time-resolution, which limits the use of this approach in many cases (including the cases studied here).

Alternatively, the effective hygroscopicity parameter can be retrieved using κ-Köhler theory from aerosol size distribution and CCN concentration measurements (Jurányi et al., 2011). We first derived $D_{crit}(SS_0)$ obtained from Eq. (5), where SS_0 is the predefined instrument supersaturation. Subsequently, we substitute D_{dry} with the derived $D_{crit}(SS_0)$ in Eq. (4), and vary the κ value until the maximum SS of the Köhler curve equals SS_0. In this way, the corresponding κ is inferred. These CCN-derived κ values quantify the effective hygroscopicity of activated particles in the CCNC and show a dependency on SS.

3.3. Estimating $N_{CCN}(SS)$ from other aerosol properties

The main parameterization of CCN spectra, which is the curve that relates N_{CCN} with SS, is the power law derived by Twomey (1959):

$$N_{CCN}(SS) = C \cdot SS^k \quad (6)$$

where C and k are empirical fit parameters. The C parameter represents the CCN concentration at $SS = 1\%$ and tracks aerosol concentration variation. Thus, high values of C parameter are typically found in polluted areas with high load of aerosol particles, while low values of C are characteristic for remote sites (Jefferson, 2010). The k parameter is a dimensionless exponent and gives information about the steepness of the CCN spectra. Therefore, an aerosol population dominated by hygroscopic or big aerosol particles would have flat CCN spectra and low values of k, while steep CCN spectra and high k values are related to hydrophobic or ultrafine particles, which would need higher SS to activate as CCN. For that reason, the k parameter indicates the nature of the particles in terms of particle activation and takes values from 0.3 to 1.2, depending on the site-specific aerosol characteristics (Hegg et al., 1991).

In order to estimate CCN concentrations at a given SS (without measurements of the CCN spectra), C and k parameters in Eq. (6) were parameterized by other aerosol properties which are commonly measured and can act as proxies of relevant aerosol properties that determine the particle activation as CCN. Since the C parameter is related to aerosol loading, the scattering properties of particles were selected to correlate with C. The backscatter fraction (BSF), acting as a proxy of the particle size, was used to parameterize C. However, because the C parameter is highly influenced by aerosol concentration, therefore, the C parameter was normalized by σ_{sp} in order to eliminate this dependence. The value of σ_{sp} can be used as a proxy of aerosol concentration, as proposed by Jefferson (2010). Single scattering albedo (SSA), acting as a proxy of the hygroscopicity of aerosol because absorbing particles are related to non-hygroscopic particles, was selected to parameterize k, following the approach in Jefferson (2010). However, in this study we have not limited the analysis to PM1 and SAE > 1 as Jefferson (2010) did.

In addition to the aforementioned parameterization using aerosol optical properties, in this study we propose the use of other aerosol properties to parameterize C and k parameters. In this second case, C was correlated with aerosol number concentration above 80 nm (N_{80}, effective CCN sizes) and k was correlated with D_{geo}, which is directly related to particle size. Note that the ability of particles to activate as CCN is dominated, mainly, by particle size.

The methodology that we follow to calculate C and k from either the optical or the physical properties consists of first fitting Twomey's law (Eq. (6)) to each hourly CCNC cycle across all SS to determine the values of C and k. Fig. S1 shows an example of the CCN spectra at both measurement stations, UGR and SNS, during a SS cycle and the inferred fit parameters according to Twomey's law. This process is repeated for each SS cycle. Then, the inferred values of C and k parameters are related to the corresponding aerosol parameter using a linear least squares fit. This allows us to express C and k as linear functions of the corresponding aerosol parameter in the following manner: $C = f(Y)$ and $k = g(Z)$, where f and g are linear equations in terms of aerosol parameters Y and Z, respectively. To build the model, the dataset has been split randomly in two subsets: the first one is used to build the model and the second one to check its performance.

4. Results and discussion

In this section, we present the results showing the CCN activation properties at urban and high-alpine stations. We first provide a general characterization of CCN concentrations and activation properties together with other aerosol properties at both environments. We next analyze the diurnal variability of CCN properties at both sites aimed at identifying the sources and processes affecting CCN properties at these two different environments. Due to the interest in the contribution of NPF to CCN and the high frequency of NPF events at the high-alpine station during the measurement period, we then analyze the contribution of NPF to CCN concentrations. Finally, we explore two empirical models for predicting CCN concentrations from other aerosol measurements.

4.1. Characterization of aerosol and CCN activation properties

Table 1 and Fig. 2 summarize the main aerosol properties observed at the urban (UGR) and high-alpine (SNS) sites. The statistics shown in Table 1 are based on all data available at each site while, in Fig. 2, data are split into seasons. The mean and median values of aerosol concentration at UGR over the whole study period was around $1.2 \cdot 10^4$ cm^{-3} and 9400 cm^{-3}, respectively, which are typical values for polluted urban environments (Che et al., 2016). N_{CN} at UGR was significantly higher in winter than in spring and summer, likely due to

Table 1
Mean values (±std, standard deviation), median values (μ_{50}) and percentiles 25th (μ_{25}) and 75th (μ_{75}) of the total aerosol concentration (N_{CN}), fresh Aitken mode particle concentration (N_{10-50}), geometric diameter (D_{geo}), backscatter fraction (BSF), single scattering albedo (SSA), scattering Ångström exponent (SAE) and BC mass concentration for the whole measurement period of each instrument. For UGR values in parentheses refer to coincident measurements with the CCNC (from October 2018 to May 2019).

Site	UGR				SNS			
Variable	Mean ± std	μ_{50}	μ_{25}	μ_{75}	Mean ± std	μ_{50}	μ_{25}	μ_{75}
N_{CN} (cm^{-3})	12000 ± 9000 (13500 ± 10000)	9400 (10000)	6100 (6300)	15000 (17500)	2600 ± 2700	1700	800	3200
N_{10-50}(cm^{-3})	7000 ± 6000 (8100 ± 7000)	5400 (6200)	3100 (3600)	8900 (10000)	1600 ± 2200	700	300	180
D_{geo} (nm)	43 ± 14 (43 ± 15)	41 (40)	32 (32)	51 (51)	62 ± 23	61	45	76
BS F (450 nm)	0.16 ± 0.06	0.15	0.13	0.16	0.14 ± 0.07	0.13	0.12	0.15
SSA (637 nm)	0.70 ± 0.10	0.72	0.62	0.79	0.92 ± 0.04	0.93	0.90	0.95
$SAE_{550-700}$	2.1 ± 0.8	2.2	1.8	2.4	1.5 ± 0.6	1.6	1.0	1.9
BC ($\mu g/m^3$)	2.0 ± 2.0 (2.3 ± 2.4)	1.3 (1.4)	0.7 (0.8)	2.5 (2.9)	0.2 ± 0.1	0.2	0.1	0.3

additional anthropogenic aerosol sources such as domestic heating and predominance of weak winds and lower atmospheric boundary layer heights (Lyamani et al., 2012). As expected, during the summer, SNS exhibits a much lower particle concentration than UGR (mean value of 2600 cm^{-3} at SNS compared with a mean value of 9400 cm^{-3} at UGR). The aerosol concentration at SNS is higher compared to other European mountain stations like Schneefernerhaus station at Zugspitze (2650 m a.s.l. in German Alps) with a median value of 1000 cm^{-3} in the diameter range from 10 to 600 nm for the period 2004–2007 (Birmili et al., 2009), or Jungfraujoch (3580 m a.s.l. in central Swiss Alps) with annual median CN concentrations of 320 cm^{-3} in the diameter range from 16 to 570 nm (around 600 cm^{-3} during summer) (Jurányi et al., 2011). However, at a lower-altitude mountain site (Puy de Dôme, France, 1465 m a.s.l), particle concentration ranged from 3200 to 4000 cm^{-3} during summer in the diameter range from 10 to 500 nm (Venzac et al., 2009). The observed particle concentration at mountain sites is highly influenced by the altitude of the sampling site and the season. Our analysis at SNS only covers the summer season, which is the period when the aerosol concentration achieves its maximum due to the high NPF event frequency and the transport of pollutants from Granada city to Sierra Nevada station as a result of mixing layer growth and mountain-valley breeze transport (Casquero-Vera et al., 2020). The concentration of particles in the diameter range 10–50 nm ($N_{10-50,}$ fresh Aitken mode particles), which are difficult to activate at low *SS*, represent more than 50% of total aerosol concentration at both sites during both experimental campaigns (Table 1).

There are also differences in the calculated intensive optical properties at the two sites, indicating the presence of different aerosol types at both sites (Table 1). The aerosol population is dominated by scattering particles at SNS, with SSA value close to 1, while at UGR the mean SSA of 0.7 reveals the strong contribution of absorbing particles. High SAE values at UGR indicate a large predominance of small particles in the urban area while the relatively low SAE values observed at SNS indicate an increased contribution of large particles to the total aerosol population over this remote station. This difference in SAE values between stations is partly due to the different measurement period at both sites

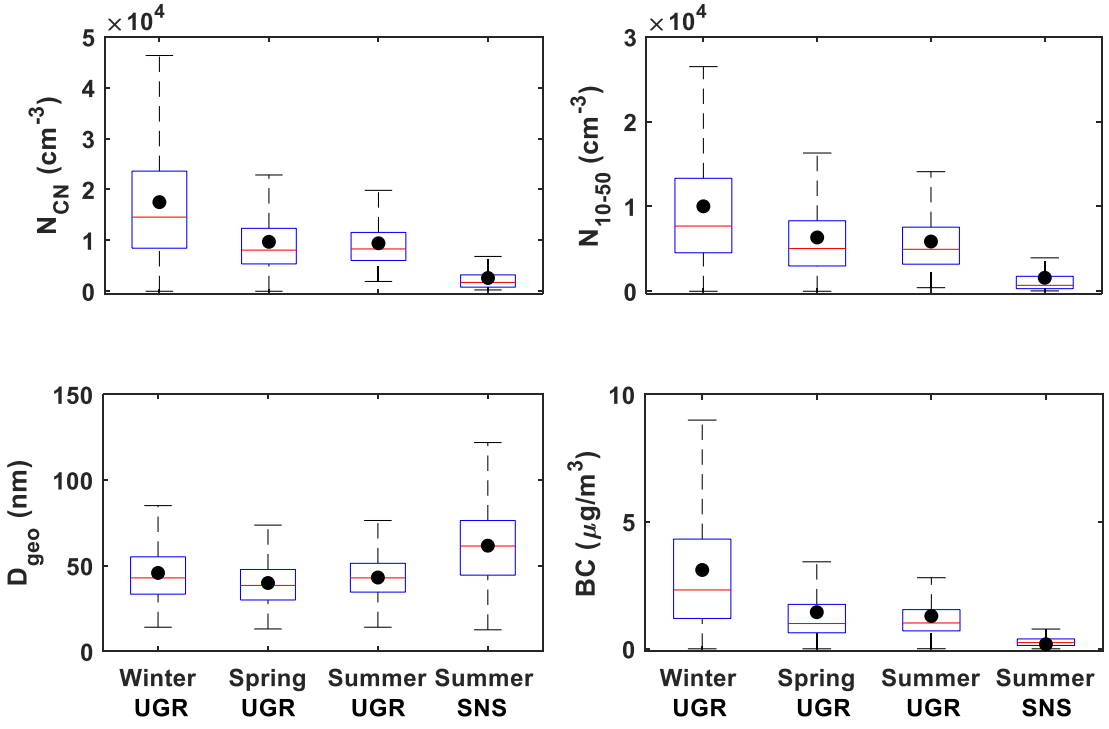

Fig. 2. Seasonal variation of aerosol concentration (N_{CN}), fresh Aitken mode concentration (N_{10-50}), geometric diameter (D_{geo}) and BC mass concentration at UGR and summer data at SNS. Mean values (black dots), median values (red lines), 25th–75th percentiles (blue boxes) and maximum-minimum values (whiskers) are presented.

(winter-spring at UGR and summer at SNS). The relatively low summer SAE values at SNS are associated with the increased frequency of Saharan dust intrusions over the study area (Valenzuela et al., 2012). BSF values at UGR (mean value of 0.16) are slightly higher than at SNS (0.14), also indicating the presence of larger particles at SNS that backscatter radiation less effectively than small particles. Using D_{geo} as a proxy for aerosol size distribution, Fig. 2 suggests that SNS is characterized during summer by the presence of larger particles (mean D_{geo} of 62 nm) than those present at UGR during (mean D_{geo} remains below 50 nm in all seasons). D_{geo} at SNS also exhibits high variability which suggests changes in aerosol sources and strength. This is consistent with the SAE values in Table 1 and can be explained by the higher influence of small freshly emitted particles at UGR compared to SNS and the seasonal impact of dust at SNS.

The BC concentrations observed at the two sites are very different, with BC at SNS station approximately an order of magnitude lower than at the urban UGR station (Table 1 and Fig. 2). BC is considered a good tracer of road traffic emissions (Lyamani et al., 2011; Reche et al., 2011). The high BC mass concentrations at UGR are mainly linked to the significant impact of local anthropogenic emissions, primarily from road traffic (Lyamani et al., 2011). BC mass concentrations at UGR are in the range of those observed at other European urban sites (Reche et al., 2011), showing higher BC concentrations and variability during winter compared to spring and summer. In contrast, the low BC concentration at SNS reflects the low influence of anthropogenic emissions at this remote site. SNS station exhibits slightly higher BC concentrations than other European mountain stations probably due to the larger influence of anthropogenic pollutants transported from Granada city to SNS station. The SNS BC values are slightly lower than those obtained at La Parva (2800 m a.s.l) in the Andes mountain range during the summer of 2015 where BC mass concentration reached values between 0.3 and 0.5 μg/m^3 (Gramsch et al., 2020). Even higher BC concentrations have been observed at similar high altitude stations in the Himalayan mountain range, such as Astore (2600 m a.s.l) and Skardu (2680 m a.s.l) stations where BC concentrations were around 1.5 μg/m^3 during August of 2017 and 2.0 μg/m^3 during September of 2017, respectively (Zeb et al., 2020). The high BC concentrations reported in the Himalayan study are due to the higher influence of anthropogenic activities compared to those affecting SNS. The study of Ripoll et al. (2015) carried out at Montsec (1570 m a.s.l.) in the pre-Pyrenees in eastern Spain showed that the mean BC value was 0.2 μg/m^3 during summer 2011, which is more similar to the BC concentration measured at SNS.

The CCN-related parameters at the two sites also exhibit significant differences. Fig. 3 shows the results for both stations in terms of CCN concentration (N_{CCN}), activation fraction (AF), critical diameter (D_{crit}) and hygroscopicity parameter (κ). CCN concentration was much higher at UGR than at SNS. Mean values of N_{CCN} at $SS = 0.5\%$ for SNS and UGR were 820 ± 600 and 2500 ± 2000 cm^{-3}, respectively. UGR exhibited a higher variability in N_{CCN} (wider interquartile range) than at SNS due to the large variability of the source emissions (mainly of anthropogenic origin) affecting UGR (Fig. 3). CN and CCN concentrations at UGR show their maximum values during winter (mean winter values of N_{CN} ~$2 \cdot 10^4$ cm^{-3} and N_{CCN} ~ 5000 cm^{-3}) compared to spring (mean spring values of N_{CN} ~ 10^4 cm^{-3} and N_{CCN} ~ 1600 cm^{-3}) due to additional emission sources (as domestic heating) and formation of thermal winter inversions that contribute to high aerosol concentrations close to the surface during winter (Lyamani et al., 2012). During winter time,

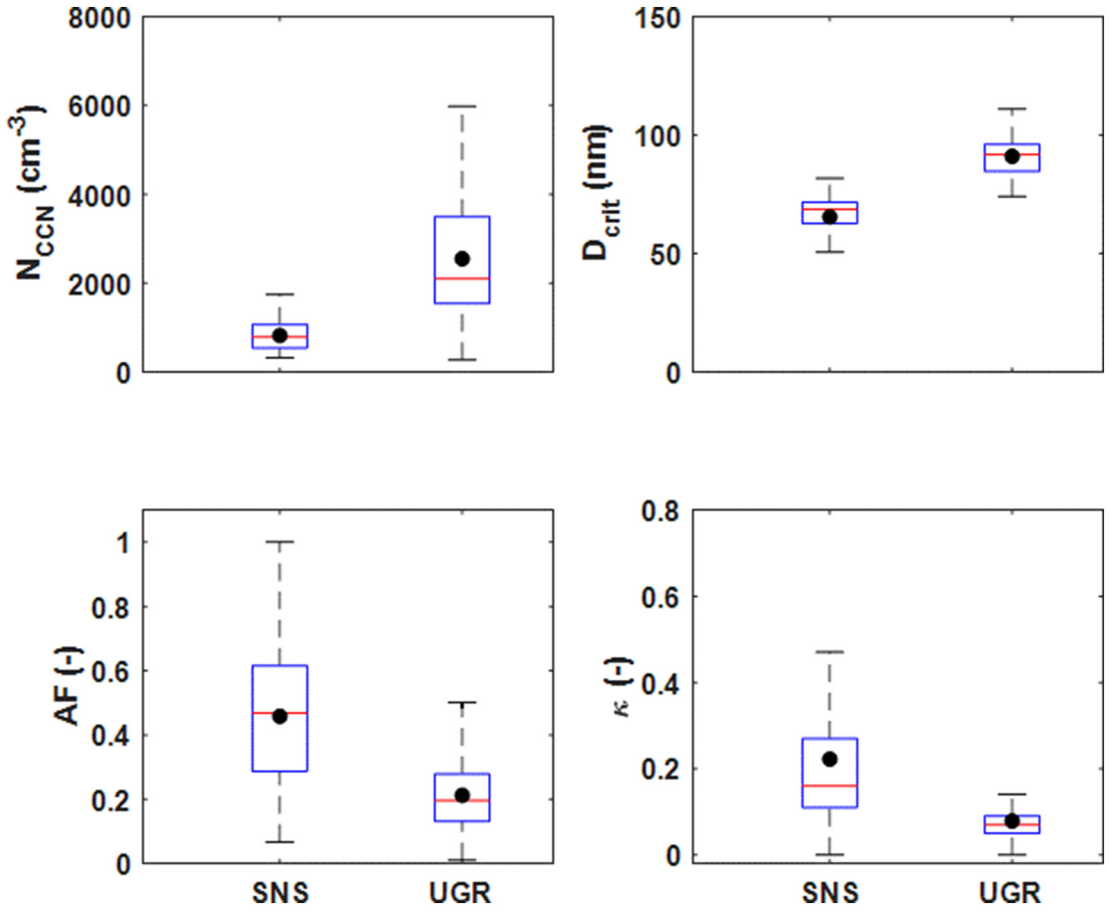

Fig. 3. Mean values (black dots), median values (red lines), 25th–75th percentiles (blue boxes) and maximum-minimum values (whiskers) of CCN concentration (N_{CCN}), Activation fraction (AF), D_{crit} and κ at UGR and SNS for all data. All measurements and inferred parameters are obtained at SS = 0.5%.

N_{CCN} concentrations at UGR are higher than those observed in Paris (2248 cm^{-3} at $SS = 0.5\%$; Jurányi et al., 2013) and similar to those values observed in big cities such as Beijing during fresh pollution conditions (4982 cm^{-3} at $SS = 0.46\%$; Gunthe et al., 2011) or Seoul (5323 cm^{-3} at $SS = 0.6\%$; Kim et al., 2014). CCN concentrations at SNS are also higher than those observed at a comparable mountain site like Jungfraujoch (313 cm^{-3} at $SS = 0.47\%$; Jurányi et al., 2011).

The mean critical diameters, $D_{crit}(SS = 0.5\%)$, obtained at UGR and SNS for the whole period were 91 and 66 nm, respectively. At a constant *SS*, a smaller D_{crit} is expected for more hygroscopic particles. Therefore, the larger D_{geo} and smaller $D_{crit}(SS = 0.5\%)$ observed at SNS compared to UGR suggest that the aerosol particles at SNS are more hygroscopic and thus can be activated more easily than those at UGR. Also, the activation fraction (AF) at a specified *SS* relates the particles that have been activated to the total amount of particles. Low values of AF at $SS = 0.5\%$ (Fig. 3) were observed at UGR, with an interquartile range of 0.13 to 0.28 and a median value of 0.20. Higher values were obtained at SNS, with an interquartile range of 0.29 to 0.62 and a median value of 0.47. The high D_{crit} and the high fraction of non-hygroscopic particles (low value of SSA) at UGR may explain the low AF values observed at this site. At UGR, characterized by low AF (values extending below 0.1), the BC concentrations were high (maximum values were close to 9 $\mu g/m^3$), whereas at SNS the opposite relationship occurs (i.e., low BC concentrations and higher AF were observed). This is consistent with fresh emitted BC being associated with small and non-hygroscopic particles. In addition, the AF shows much more variability (wider interquartile range) at SNS, despite the narrow interquartile range of N_{CCN}. This might be due to the significant changes in aerosol size distribution during the study period at SNS, as evidenced by D_{geo} variability (Fig. 2). Casquero-Vera et al. (2020) found that NPF events are very frequent at SNS during summer time, which enhances the total number concentration of particles and shifts the size distribution towards smaller sizes. This phenomenon together with the aerosol transport from Granada city to SNS can contribute to the large variability observed in AF at SNS.

Inferring the hygroscopicity parameter κ from CCN and size distribution measurements (see Section 3.2) allows us to quantify the overall hygroscopicity of activated particles, which provides qualitative information on the bulk aerosol composition. The estimated mean value of κ at $SS = 0.5\%$ was 0.08 ± 0.03 at UGR (ranging from 0.05 to 0.09), and 0.22 ± 0.09 at SNS (ranging from 0.11 to 0.27). This result is consistent with the D_{crit} behavior described previously which suggested lower hygroscopicity at the urban site compared to the high-alpine site. The higher variability of κ observed at SNS compared to UGR (see Fig. 3) may be explained by the higher variability in aerosol properties at SNS which is affected by (i) air masses from different origins, (ii) NPF events that significantly affect the size distribution and (iii) the influence of atmospheric boundary layer (ABL) dynamics that transport pollutants from the Granada area to Sierra Nevada. In contrast, aerosol particles at UGR are strongly dominated by local sources, especially road traffic, leading to an overall non-hygroscopic aerosol. Relatively lower mean values of κ are observed at UGR in winter season ($\kappa = 0.06 \pm 0.01$) compared to spring ($\kappa = 0.09 \pm 0.02$) (not shown here). Previous studies at UGR have shown the low hygroscopicity of aerosol particles at this site due to the predominance of absorbing particles composed of species such as BC and organic matter, especially during winter (Titos et al., 2014b; Burgos et al., 2019). The mean κ parameter at SNS is higher than at UGR but it is below 0.3, which is the typical value associated with continental background aerosol (Andreae and Rosenfeld, 2008), suggesting there is an impact of anthropogenic aerosol at SNS as well.

Table 2 shows a comparison of N_{CCN}, AF, D_{crit} and κ values from the literature and those obtained in this study for SNS and UGR. Compared with the studies listed in Table 2, among the urban sites, UGR is characterized by the lowest κ parameter and one of the highest D_{crit} values, demonstrating the hydrophobic nature of aerosol particles at UGR during winter and spring seasons, and consequently low activation capacity. Results obtained at SNS are consistent with those values reported at Jungfraujoch (3580 m a.s.l.) and Puy De Dôme (1465 m a.s.l.) during summer (Table 2), with very similar AF, D_{crit} and hygroscopicity parameter values.

4.2. Diurnal evolution patterns

In the previous section, overall differences in activation properties in relation to other aerosol properties between the two sites were discussed. Here we evaluate the impact of temporal patterns, specifically the diurnal cycle of CCN. Analyzing the diurnal evolution of the activation properties of aerosols can be useful for understanding the sources and transformation processes at the urban and high-mountain sites. Fig. 4 shows the diurnal evolution of aerosol size distribution, N_{CCN}, N_{CN}, BC, AF, SSA, D_{crit} and D_{geo} at both stations. Note that the scales in Fig. 4 are different for UGR and SNS to allow better visualization of the diurnal patterns and N_{CCN} and N_{CN} are both referred to the left Y axis in

Table 2
Summary of activation parameters for each measurement location. For all studies listed, the hygroscopicity parameter corresponds to the parameter calculated from CCN measurements. In addition, relevant information about the campaigns are listed in the table.

Site location	Period	SS (%)	N_{CCN} (cm^{-3})	AF (−)	D_{crit} (nm)	κ (−)	Diameter range	Reference
Urban								
Vienna, Austria	Interannual	0.50	820	0.13	162	–	13–929	Burkart et al. (2011)
Hong Kong, China	Spring	0.50	1815	0.57	56	0.31	7–300	Meng et al. (2014)
Paris, France	Winter	0.50	2248	–	76	0.11	10–413	Jurányi et al. (2013)
Granada, Spain	Winter/spring	0.50	2500	0.21	91	0.08	10–514	This study
KORUS-AQ, South Korea	Spring	0.60	3373	0.31	–	0.22	>10	Kim et al. (2018)
Seoul, South Korea	Interannual	0.60	5323	0.30	–	–	10–414	Kim et al. (2014)
Beijing, China	Summer	0.46					3–800	Gunthe et al. (2011)
Aged pollution			8830	0.74	59	0.31		
Fresh pollution			4980	0.25	74	0.18		
Rural/remote								
Princess Elisabeth station, Antarctica	Summer	0.50	177	0.51	–	–	>3	Herenz et al. (2019)
Amazon Basin, Brazil	Annual	0.47	883	0.74	77	0.13	10–450	Pöhlker et al. (2016)
Noto Peninsula, Japan	Autumn	0.52	–	–	60	0.24	–	Iwamoto et al. (2016)
Cape Fuguei, Taiwan	Spring	0.54	1689	0.59	54	0.22	13–736	Cheung et al. (2020)
Finokalia, Crete	Summer	0.51	2003	0.80	–	0.34	20–460	Bougiatioti et al. (2011)
Yangtze river delta, China	Annual	0.45	6271	0.62	62	0.28	20–300	Che et al. (2017)
Mountain								
Jungfraujoch, Switzerland	Summer	0.57	313	0.53	68	0.17	16–570	Jurányi et al. (2011)
Sierra Nevada, Spain	Summer	0.50	820	0.47	66	0.22	10–514	This study
Puy de Dôme, France	Summer	0.51	200–2000	–	65	0.22	10–400	Asmi et al. (2012)

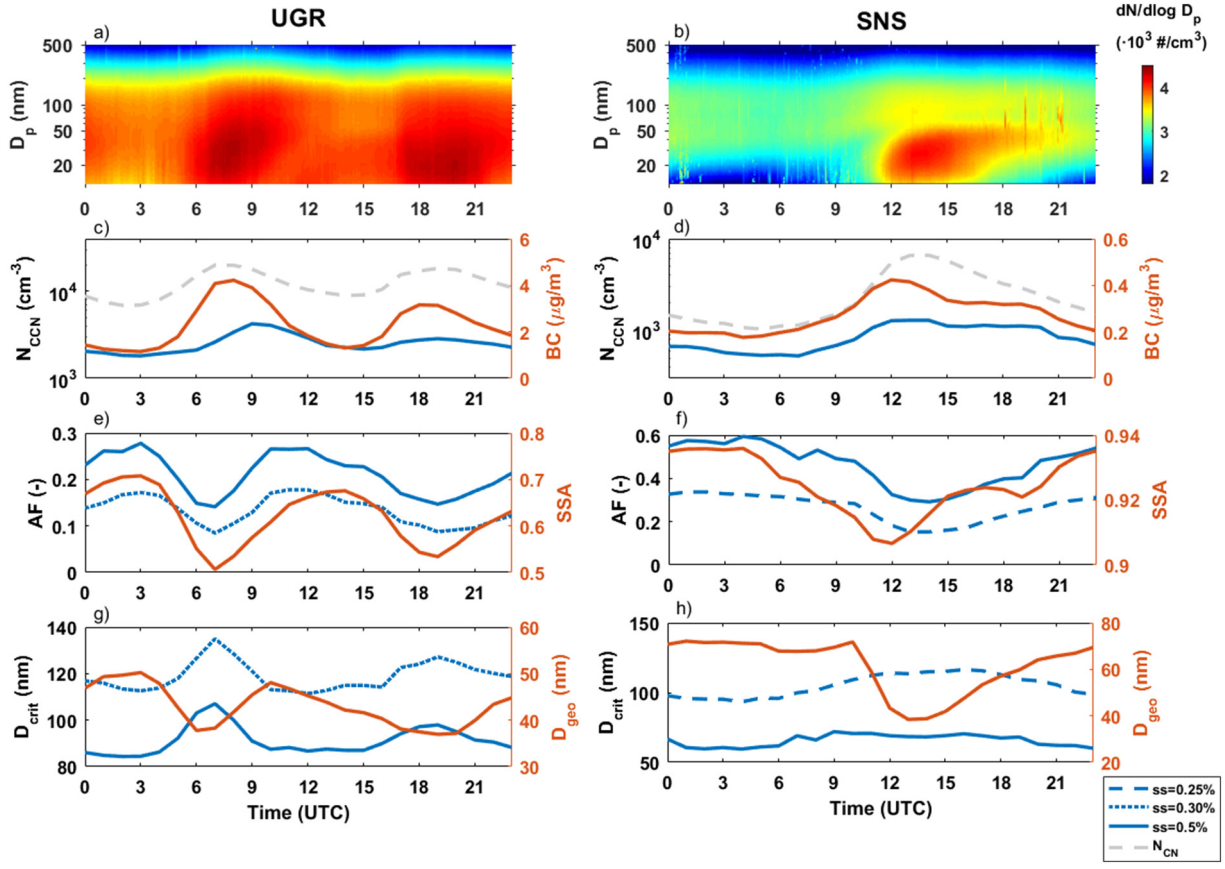

Fig. 4. Diurnal patterns of aerosol size distribution, N_{CCN}, N_{CN}, AF, SSA at 637 nm, D_{crti} and D_{geo} obtained at UGR station (left panels) and SNS station (right panels). N_{CCN} and N_{CN} are both referred to the Y axis on the left in Fig. 4c and d.

Fig. 4c and d for a better comparison. BC has been used here as tracer of road traffic emissions and SSA as an estimation of the relative contribution of absorbing particles (mainly BC) to the total aerosol load.

The mean diurnal evolution of the aerosol size distribution at both sites is shown in Fig. 4a and b. The aerosol concentration at UGR is dominated by particles below 100 nm during the whole day. Between 06:00 and 09:00 UTC and 18:00 and 21:00 UTC, during the traffic rush hours, the particle concentration increased noticeably in all sizes, but especially in the diameter range from 10 to 50 nm. At SNS, we can observe a completely different behavior of the aerosol size distribution. Before 12:00 UTC, at SNS particles are mainly confined in the size range 20–200 nm and are characterized by low number concentration. At around 12:00 UTC a clear mode of particles between 10 and 50 nm appears. From 12:00 UTC and onwards, this mode grows to larger sizes and then decreases in intensity throughout the rest of the day. This pattern suggests that NPF events occurring at midday influence the aerosol size distribution at SNS.

As can be seen in Fig. 4c, the BC diurnal pattern is characterized by two maxima at UGR during traffic rush hours while, at SNS, BC is characterized by a maximum at midday associated with the upslope transport of pollutants from Granada area to SNS (Fig. 4d). At both sites, N_{CN} and N_{CCN} exhibit similar patterns to BC. At UGR, the diurnal evolution of N_{CN} shows two maxima during the day coinciding with traffic rush hours (peak values were $(2.0 \pm 1.3)\cdot 10^4$ and $(1.8 \pm 0.9)\cdot 10^4$ cm^{-3} at 7:00 and 19:00 UTC). N_{CCN} also exhibits two maxima with peaks values of 4200 ± 3000 and 2800 ± 2000 cm^{-3} but at different time: 9:00 and 19:00 UTC. The delay observed between the morning peaks of N_{CCN} and N_{CN} might be caused by the fact that particles emitted by road traffic with diameter below the D_{crit} are able to grow to larger diameters above D_{crit} in the following hours (particles reach around 90 nm at 10:00 UTC), and act as CCN. Also, oxidation of emitted particles can affect the aerosol hygroscopicity leading to higher N_{CCN}. This is supported by the observed increase in κ (Fig. 5) in coincidence with N_{CCN} after traffic rush hours. The combination of both processes could explain the delay observed between the morning peaks of N_{CCN} and N_{CN}. The lack of such a time delay between the evening peaks N_{CCN} and N_{CN} may be due to differences in the observed aerosol properties for the morning and evening periods. As a consequence of the diurnal evolution of N_{CN} and N_{CCN}, AF at UGR shows two minima during the day at 7:00 and 19:00 UTC. SSA diurnal evolution also shows two minima that coincide with the AF minima, denoting an increase in the contribution of absorbing particles (mostly hydrophobic particles) that are not activated. It is interesting to note that the AF diurnal range (difference between the maximum and minimum values) increases with *SS*. This behavior is likely due to the fact that outside of traffic rush hours, higher *SS* values result in higher CCN concentration; however, during traffic rush hours the same *SS* increase in the instrument rarely increases CCN concentration due to the high concentration of ultrafine and BC particles, which are extremely difficult to activate even at high *SS*. D_{geo} values at UGR also exhibit a diurnal pattern with two minima at traffic rush hours, with values below 40 nm. In urban environments, road traffic emissions are the main source of ultrafine particles. These two D_{geo} minima, then, are likely attributed to newly formed particles due to emission of precursor gases by road traffic. Conversely, the D_{crit} diurnal pattern shows two maxima for all *SS* values that coincide with the D_{geo} minima during traffic rush hours. The D_{crit} peaks during traffic rush hours are related to the emission of aerosol particles with a more hydrophobic chemical composition (such as BC). Even if the diameter of these recently emitted particles is above the D_{crit}, these particles are unable to activate due to their chemical composition and hygroscopicity properties. This leads to an increase in the D_{crit} value when it is calculated using Eq. (4) (backward integration of the aerosol size distribution).

At SNS, the diurnal behavior is completely different (Fig. 4). N_{CN} and N_{CCN} at *SS* = 0.5% exhibit a maximum between 13:00 and 14:00 UTC with mean values around 6500 ± 4000 and 1300 ± 800 cm^{-3}, respectively. The BC diurnal pattern, used as a proxy of anthropogenic pollution at SNS, has its maximum earlier, at 12:00 UTC. This increase in BC at midday is associated with the diurnal evolution of the ABL and upslope transport of pollutants from the valley to the high mountain station. As Moreira et al. (2020) showed using microwave radiometer and ceilometer measurements, the ABL height in Granada starts increasing in the morning and achieves its maximum at midday, reaching the SNS station height at midday during the summer. In addition to the increase in height of the ABL over Granada, the westerly winds that predominate during the day at SNS favor the transport of pollutants from the valley to the mountain (Casquero-Vera et al., 2020). N_{CN}, N_{CCN} and BC start increasing at around 8:00 UTC, but as mentioned before, the maximum is achieved later for N_{CN} and N_{CCN} than for BC. This timing difference between BC and N_{CN} suggests an additional source of N_{CN} other than transport from Granada to Sierra Nevada. Unlike at UGR, at SNS the AF and SSA do not follow the same diurnal pattern. The SSA minimum occurs earlier (at 12:00 UTC) than the AF minimum (14:00 UTC). Therefore, the increase in the relative contribution of absorbing particles might not be the main factor controlling N_{CCN} and AF at SNS. The D_{geo} diurnal pattern shows a sharp decrease at midday (between 12:00 and 14:00 UTC) which is associated with the high frequency of NPF events that occur at midday during summer (Casquero-Vera et al., 2020). Although the transport of anthropogenic particles from Granada area also may affect D_{geo}, the sharp D_{geo} decrease observed and the shorter duration of this decrease (as compared with the BC increase) suggests that NPF events might be the main source of particles at SNS at midday.

D_{crit} does not show a clear diurnal pattern at SNS, except at *SS* = 0.25%, the lowest *SS* studied. At this *SS*, there is a wide increase from 08:00 UTC and onwards, with a maximum around 14:00 UTC. This increase in D_{crit} may be associated with the lower hygroscopicity of the predominant particles at this time of the day, which are a combination of particles transported upslope from the Granada urban area and newly formed particles after growth (Casquero-Vera et al., 2020). The different behavior of D_{crit} with different *SS* values is interesting. At higher *SS*, D_{crit} is roughly constant throughout the day, in contrast to the behavior of D_{crit} at lower *SS*. At lower SS, there are particles which are less hygroscopic that do not activate while those particles are able to activate at higher SS. At midday, the transport of particles could lead to overall lower aerosol hygroscopicity as shown in Fig. 5. Note also the increase in BC mass concentration and decrease in SSA at midday.

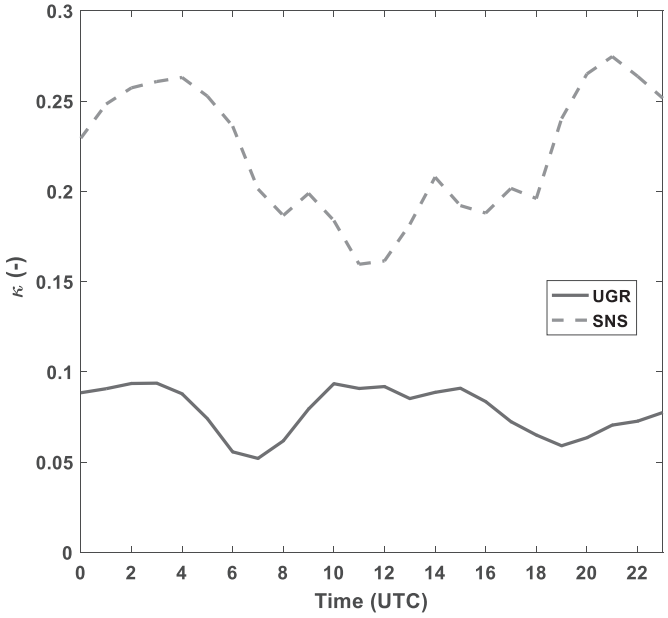

Fig. 5. Diurnal pattern of kappa parameter at UGR and SNS at SS = 0.5%.

Fig. 5 shows the diurnal cycle of the hygroscopicity parameter κ. The hygroscopicity parameter is a proxy for the size and chemical composition of the whole population of activated particles. At UGR, κ shows two diurnal minima associated with road traffic emissions (Fig. 5). During traffic rush hours, κ decreases due to the increase of non-hygroscopic particles and UFP concentration (mainly nucleation and fresh Aitken mode particles). There is a decreasing trend of κ as *SS* increases (not shown). This is because the less hygroscopic particles are activated when *SS* increases; κ approaches 0.05 during traffic rush hours. At SNS, during the first and last hours of the day, κ has values around 0.25. At 10:00 UTC, κ starts to decrease coincident with the increase observed in BC concentration and the decrease in D_{geo}. κ achieves its minimum at 12:00 UTC with a value of 0.16 (Fig. 5). This is consistent with changes in aerosol chemical composition and size due to NPF and the transport of aerosols from Granada city to Sierra Nevada leading to a reduction of κ value.

These results suggest that the two main aerosol sources influencing activation properties of aerosols at SNS during summer are newly formed particles due to nucleation events and the transport of pollutants from Granada. As these two processes seem to occur simultaneously around midday, our observations reflect the joint effect of both processes. In order to understand the behavior of activation properties during NPF events, in the following section we analyze the contribution of NPF to CCN in Sierra Nevada.

4.3. Contribution of NPF to CCN in Sierra Nevada

To perform this analysis, we classified by visual interpretation the number aerosol size distributions measured at SNS as NPF events, non-events, undefined and bad-data days following the procedure proposed by Dal Maso et al. (2005). During the measurement campaign at SNS 67 NPF events, 16 undefined events and 13 non-events days were observed. However, not all NPF events showed the typical "banana shape" associated with particle growth. Following Rose et al. (2017) criteria, only those NPF events referred as type I, i.e. with clear particle growth from smallest sizes, were selected to investigate the contribution of NPF events on CCN concentrations. Type II events are more irregular and may be interrupted in certain size ranges (Rose et al., 2017), and in bump type events the growth of newly formed particles is not observed (Hirsikko et al., 2007; Yli-Juuti et al., 2009). Therefore, we focused our analysis on type I events and selected the 15 clearest NPF events. Mean diurnal evolution of the aerosol size distribution is shown in Fig. S2 for event and non-event days. During event days we can observe a clear growth of particles from the lowest diameter (10 nm), which appear around 12:00 UTC, to larger diameters (around 70 nm) during the rest of the day until 21:00 UTC. During non-event days the aerosol size distribution is characterized by particles in the range 20–200 nm and after 12:00 UTC the particle concentration increases in the diameter range between 20 and 80 nm which is related to the vertical transport of particles from the urban area.

Fig. 6 shows the comparison of the diurnal evolution of N_{CCN}, N_{CN}, AF, D_{crit} and D_{geo} at SNS during NPF event (solid line) and non-event (dash line) days. There is a clear difference in all variables investigated between event and non-event days. This difference is large during the daytime hours while during the evening there is no difference between NPF and non-event days. As expected, $N_{10–20}$ and $N_{20–50}$ are the variables most affected by NPF events. Changes in their diurnal patterns are noticeable starting at 10:00 UTC, when the nucleation process tends to initiate. $N_{10–20}$ and $N_{20–50}$ maximum concentrations during NPF events are approximately 8 times higher than the corresponding values during non-event days. $N_{10–20}$ reaches its maximum at around 12:00 UTC while $N_{20–50}$ reaches it 2 h later, due to particle growth. $N_{50–100}$ is also

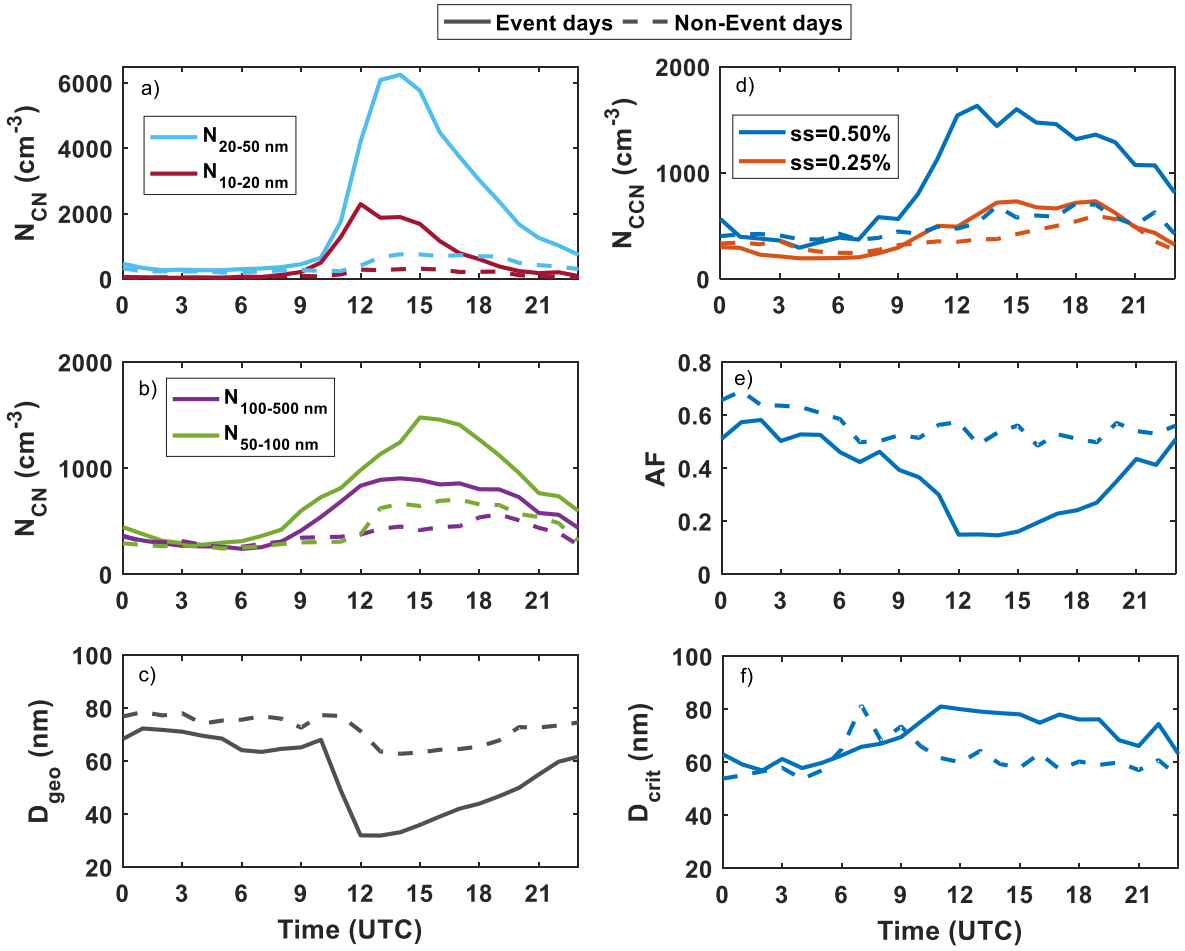

Fig. 6. Diurnal patterns of (a) and (b) N_{CN} for different diameters ranges, (c) geometric diameter, (d) N_{CCN} at different SS, (e) activation fraction and (f) critical diameter at 0.50%. Solid lines represent the average diurnal pattern for days classified as NPF event days and dash lines for non-event days at SNS station.

affected by NPF - it does not show a sharp increase as is seen for $N_{10–20}$ and $N_{20–50}$; rather it shows a constant gradual increase during the morning and afternoon until $N_{50–100}$ reaches its maximum value at 15:00 UTC. $N_{100–500}$ is the size range least affected by NPF, exhibiting the lowest difference between event and non-event days of all particle size ranges. However, this is the size range that is expected to have the most influence on the CCN concentration and activation properties at low *SS*. As we can see in Fig. 6b and d, $N_{100–500}$ and N_{CCN} at $SS = 0.25\%$ follow similar trends with maxima at 15:00 UTC.

NPF clearly contributes to the increase in N_{CCN} starting at 10:00 UTC, although its contribution is controlled by the *SS*. It is interesting to note that the difference between N_{CCN} at $SS = 0.25\%$ and $SS = 0.50\%$ is larger during NPF event days. For example, the highest value of the ratio between N_{CCN} during event and non-event days is 1.9 at $SS = 0.25\%$ (14:00 UTC) and 3.1 at $SS = 0.5\%$ (13:00 UTC). This suggests that the contribution of NPF can be an important source of CCN in Sierra Nevada especially at high *SS*. NPF events also affect the values of D_{crit}, D_{geo} and AF. These parameters show smoother diurnal patterns during non-event days than during event days (Fig. 6). D_{crit} seems to be less influenced by NPF events but showing a slight increase starting at 10:00 UTC during NPF event days (around 80 nm) compared to non-event days (around 60 nm). The diurnal pattern of D_{geo} and AF are very similar, with a marked decrease during NPF event days from 10:00 UTC and onwards, reaching their minimum at 12:00 UTC. This evolution is explained by the behavior of $N_{10–20}$ and $N_{20–50}$. As the concentration of newly formed particles increases suddenly due to nucleation, D_{geo} exhibits a sharp decrease reaching its minimum value (32 nm) at 12:00 UTC. AF has a minimum at the same time (AF = 0.15 at 12:00 UTC) due to the high concentration of very small particles that do not activate. After reaching the minimum, AF and D_{geo} start to increase their values due to particle growth during the second half of the day. During non-event days, $N_{10–20}$ and $N_{20–50}$ (typically related to anthropogenic sources), show a smooth increase starting at 12:00 UTC (Fig. 6a). This and the subsequent decrease observed in AF and D_{geo} are associated with local and transported pollution from the Granada urban area (Fig. 6c and e).

In order to estimate the contribution of NPF to CCN, isolated from other sources like transport of pollutants from Granada, we use the methodology proposed by Rose et al. (2017). This method quantifies the contribution of NPF to CCN by calculating the CCN enhancement (ΔN_{CCN}) from the comparison of N_{CCN} prior to the nucleation event and the maximum during the event. As proposed by Rose et al. (2017), ΔN_{CCN} during non-event days accounts for all CCN sources except NPF events, while ΔN_{CCN} during event days accounts for both contributions. Subtracting one from the other, we can infer the contribution of NPF to CCN alone (ΔCCN_{NPF}). This method assumes that the pre-existing particle concentration in the CCN size range at the measurement site is similar during event and non-event days (Rose et al., 2017). That appears to be the case at SNS based on Fig. 6a and b where the solid and dashed lines tend to overlap in the time period prior to the start of nucleation at 10:00 UTC.

The contribution of NPF to CCN in Sierra Nevada, according to Rose et al. (2017) methodology, was 115% and 175% at SS = 0.25% and SS = 0.5%, respectively. This suggests that NPF plays an important role

Table 3
Relative contribution of NPF to CCN activity at different locations (ΔCCN_{NPF}). In Rose et al. (2017) study CCN concentrations were not directly measured, it is marked with an asterisk. Information specifying if an individual event from long-term dataset with the maximum contribution is taken into account is also specified in the table.

Site location	Type		SS (%)	ΔCCN_{NPF} (%)	Reference
Shanghai, China	Urban		0.20	17	Leng et al. (2014)
			0.60	88	
Vienna, Austria	Urban		0.50	38	Dameto de España
		Max	0.50	143	et al. (2017)
Finokalia, Greece	Remote/marine	Max	0.35	88	Kalkavouras et al. (2019)
		Max	0.52	94	
Melpitz, Germany	Remote		0.40	66	Wu et al. (2015)
			0.60	69	
Chacaltaya, Bolivia	Mountain		–	100–250	Rose et al. (2017)*
Sierra Nevada, Granada	Mountain		0.25	115	This study
			0.50	175	

in the CCN budget at SNS, and, indeed, might be the major CCN source at higher *SS*. Table 3 summarizes the relative contribution of NPF to CCN at different sites compared to Sierra Nevada. For the comparison, it is important to bear in mind that there are several indirect approaches to estimate NPF contribution to N_{CCN} without actual in situ measurements of CCN (e.g., estimating D_{crit} from chemical composition data or just assuming a D_{crit} above which all particles activate). A lower relative contribution of NPF to CCN concentrations was observed at remote environments like Finokalia in Crete and Melpitz in Germany. Our estimations at SNS are similar to results reported by Rose et al. (2017) for Chacaltaya Mountain in Bolivia (5240 m a.s.l) where the NPF contribution to CCN ranges from 100% to 250% assuming a D_{crit} of 100 or 50 nm, respectively. In more polluted urban environments like Shanghai and Vienna, the NPF relative contribution to CCN is lower due to the impact of anthropogenic emissions. Dameto de España et al. (2017) pointed out that NPF could also be a measurable, but not very frequent source of CCN in urban environments.

4.4. Predictions of N_{CCN} from ancillary measurements

In this section, we present the results of estimating CCN concentrations from aerosol properties that are more frequently measured than CCN concentrations at most atmospheric observatories (Pandolfi et al., 2018; Schmale et al., 2018). The results of applying Twomey's law (Eq. (6)) following the methodology presented in Section 3.3 are shown in Table 4. This table shows linear fit parameters (slope of the fit and, in parentheses, the R^2 coefficient) of Twomey's law *C* and *k* parameters and aerosol optical and size distribution parameters. The results are compared with those from other sites around the world (Jefferson, 2010). The R^2 coefficients obtained for UGR and SNS are similar to those reported by Jefferson (2010) at different sites (rural, urban and marine), although in general the correlations are relatively low, especially the correlation between *k* and SSA. The normalized parameter $\boldsymbol{C/\sigma_{sp}}$, which is related to inverse aerosol scattering efficiency, increases with BSF (meaning higher contribution of fine particles) and the slopes have positive values. Jefferson (2010) suggests that higher values of the slope of $\boldsymbol{C/\sigma_{sp}}$ vs BSF can be related to higher contribution of particles with low scattering efficiency (i.e. organic matter, carbonaceous aerosols), while lower values of the slope are associated with a predominance of particles with higher scattering efficiency such as inorganic aerosols. Alternatively, using N_{80} to parameterize *C*, instead of BSF, results in significantly better R^2 values. Note that *C* is related to the CCN concentration at *SS* = 1%, therefore, *C* will increase when N_{80} does. At SNS, the calculated slope is higher than at UGR, which means that changes in N_{80} will have a bigger effect on the N_{CCN} estimates.

Table 4
Coefficients of linear fits between aerosol parameters and Twomey's law parameters. Each value represents the slope of the fit (the R^2 value is given in parentheses).

Site location	$\boldsymbol{C/\sigma_{sp}}$ vs BSF	*C* vs $\boldsymbol{N_{80}}$	*k* vs SSA	*k* vs $\boldsymbol{D_{geo}}$
Oklahoma, USA	1610 (0.50)	–	−3.78 (0.38)	–
Black Forest, Germany	1430 (0.64)	–	−3.07 (0.20)	–
Graciosa, Portugal	937 (0.33)	–	−2.24 (0.23)	–
Hefei, China	1450 (0.22)	–	−1.73 (0.07)	–
Granada, Spain	1358 (0.40)	0.99 (0.83)	−0.33 (0.03)	0.005 (0.05)
Sierra Nevada, Spain	2183 (0.49)	1.03 (0.77)	−3.52 (0.09)	0.006 (0.12)

Parameterizing *k* is more challenging, because it is difficult to relate it to other physical or optical properties of the particles. This is reflected in the table showing that the R^2 values are lower for all sites for this parameterization, with no correlation ($R^2 < 0.15$) at both Granada and Sierra Nevada. Fitting *k* vs SSA yields negative slopes because, as absorbing particle concentration increases, changes in N_{CCN} with *SS* are lower, principally at low *SS*. It is caused by absorbing particles like BC that remain non-activated at all *SS* values. Remote sites with low concentration of BC particles and relatively high SSA, such as Oklahoma, Black Forest or Sierra Nevada, show the highest absolute values of the slope. Conversely, sites influenced by pollution, with lower SSA, are associated with lower absolute values of the slope (i.e., Hefei and Granada). Using the alternative approach proposed in this study to parameterize *k* based on size distribution measurements (D_{geo}) does not result in better correlations than those observed with the Jefferson (2010) approach. Despite Jefferson (2010) limiting the study to SAE > 1 and PM1 particles, fit parameters at UGR and SNS are within the range of values reported in Jefferson (2010) as can be seen in Table 4.

In order to evaluate the ability of the two empirical models to estimate CCN concentrations at Granada and Sierra Nevada, we determined the empirical coefficients using 50% of data and used the remaining data for evaluation. In order to diminish any possible seasonal pattern that might appear in building the model, especially in UGR, we split the data randomly in two subsets, one set is used to build the model and the other one to test it. Fig. 7 shows the validation of the empirical model proposed by Jefferson (2010) applied to the UGR and SNS datasets. The model provides satisfactory results for Granada. The averaged ratios of predictions vs measurements are: 1.24 at 0.3% and 1.14 at 0.9% *SS*. At UGR the slopes are close to 1 and the R^2 values are close to 0.8 indicating that the model can explain the measurements. The dispersion of data remains roughly constant as *SS* increases. The model does not show a clear bias due to different values of SSA because data are distributed uniformly according to their SSA value (Fig. 7). At SNS, the model does not provide satisfactory results. Mean values of predictions versus measurement ratios show that this method overestimates the CCN measurements (1.45 for *SS* = 0.25% and 1.54 for *SS* = 0.7%). The slope and R^2 coefficients are very low in this case and there is wide dispersion of the data because the model is unable to estimate N_{CCN} at SNS when there is a high value of the SSA (Fig. 7). Additionally, neither the slope nor the R^2 values improve significantly for higher *SS* values. Since there is no correlation between the *k* parameter and SSA, the model is not able to reproduce the observed changes in the SSA.

The alternative empirical model based on N_{80} and D_{geo} provides better results at the two stations, except at low *SS* value at SNS (Fig. 8). At UGR, this model also provides satisfactory results with values of the slope relatively close to 1 and R^2 close to 0.8. The averaged ratio of predictions and measurements (1.23 at 0.3% and 1.27 at 0.9% *SS*) were similar using this model and the Jefferson (2010) model. At UGR, high CCN concentrations are directly related to large values of the D_{geo}. Also this model based on N_{80} and D_{geo} is better at reproducing the observations at SNS. In this case, the ratio of predictions vs measurements was 1.24 and 1.29 for *SS* = 0.25% and 0.7%, respectively. The slope and R^2 values show a large improvement at high *SS* (0.99 and 0.81, respectively) compared to low *SS* (0.54 and 0.38, respectively). As mentioned in Section 4.2, SNS is highly influenced by NPF events and vertical

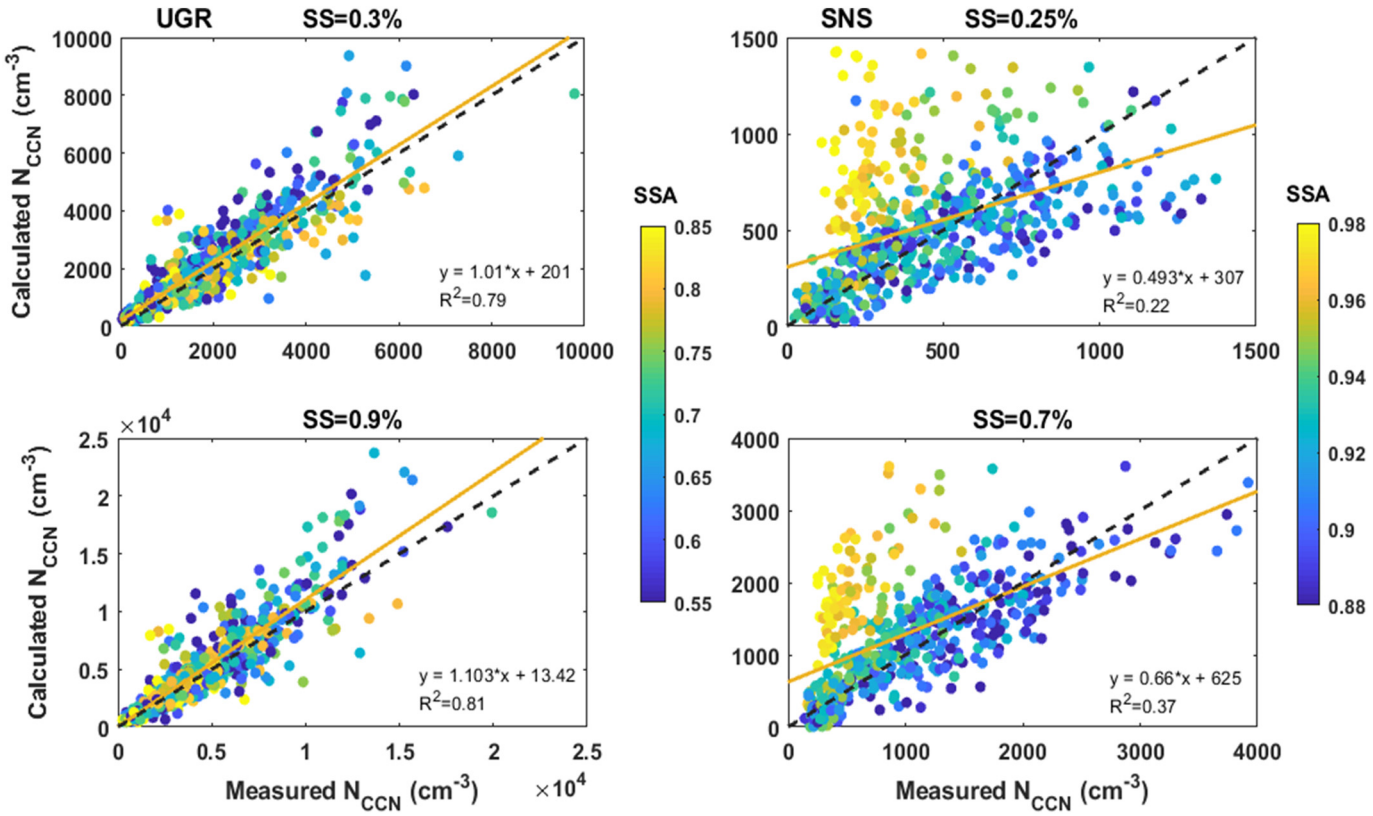

Fig. 7. Correlations between calculated vs measured N_{CCN} for UGR (left panels) and SNS (right panels) at two supersaturations, color-coded as a function of single scattering albedo (SSA) at 637 nm. Least squares fit and 1:1 line are shown on each graph.

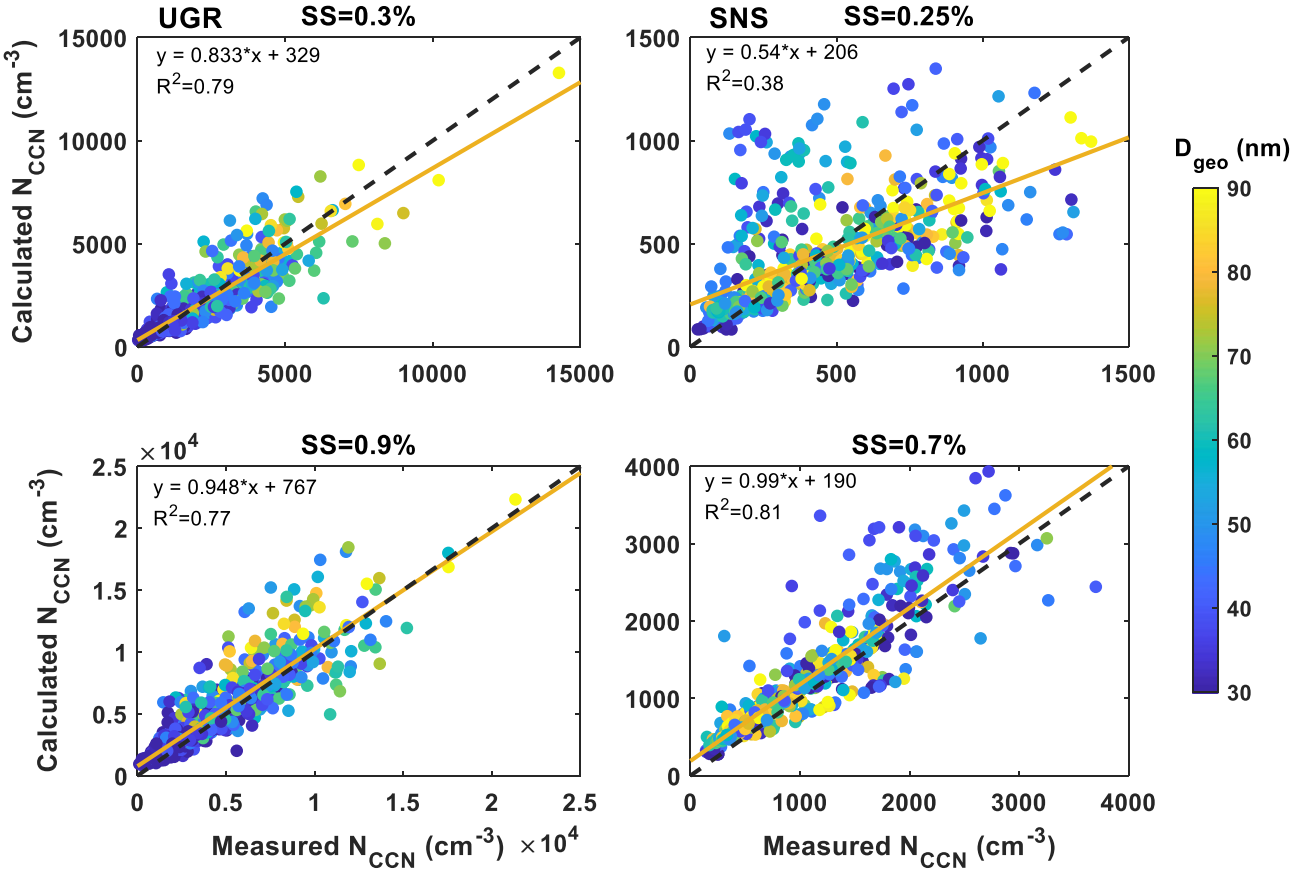

Fig. 8. Correlations between calculated and measured CCN at UGR (left panels) and SNS (right panels), color-coded as a function of D_{geo}. Least squares fit and 1:1 line are shown on each graph.

transport of particles from UGR occurring at midday. These two phenomena could contribute significantly to N_{80}, but at $SS = 0.25\%$ barely contribute to N_{CCN}. However, at higher $SS = 0.7\%$ these two phenomena contribute to N_{CCN} and the model reproduces measurements much better than at lower SS (Fig. 8). As can be seen in Fig. 8 for SNS, low values of D_{geo} (bluish colors) deviate from the 1:1 line and are more disperse.

Using empirical models, which parameterize Twomey's power law parameters in terms of aerosol properties to predict N_{CCN} remains a difficult challenge. The two empirical models used here are not able to reproduce the measurements in all cases at the two sampling stations; however, it appears that the empirical model based on physical aerosol properties provides a better approach for predicting CCN. The empirical model based on aerosol optical properties provided satisfactory results at UGR, but showed low correlations at the mountain station between calculated and measured N_{CCN} ($R^2 < 0.4$).

5. Conclusions

This study analyzes the first CCN in-situ measurements performed in the Iberian Peninsula. Measurements were carried out at two different sampling stations: an urban background station (UGR, 680 m a.s.l.) located in the city of Granada and an alpine station (SNS, 2500 m a.s.l.) that is influenced by emissions from the urban area. Measurements of CCN concentration, aerosol light scattering, backscattering and absorption coefficients and black carbon mass concentrations were obtained for the period from October 2018 to end of May 2019 at UGR and from June to end of August 2019 at SNS. Also, measurements of aerosol size distribution in the diameter range 10–514 nm were measured for the period from October 2018 to end of August 2019 at UGR and from June to end of August 2019 at SNS.

At UGR, the N_{CCN} mean value at $SS = 0.5\%$ was 2500 ± 200 cm^{-3} and the mean value of N_{CN} in the diameter range of 10–514 nm was around $13{,}000 \pm 9000$ cm^{-3} with $D_{geo} = 45$ nm; consistent with typical values of urban environments. Because the D_{crit} at all SS values remained above D_{geo} and was associated with high concentration of BC particles, which are highly non-hygroscopic particles, UGR exhibited extremely low AF (at $SS = 0.5\%$ AF is around 0.21 ± 0.11) similar to other urban environments. CCN-derived κ values averaged during the whole UGR campaign ranged from 0.05 to 0.01 at $SS = 0.50\%$. The low κ value is associated with the high contribution of BC particles with low hygroscopicity (κ close to 0), showing the lowest κ values during winter (from December to February) when the BC concentration peaks. The diurnal evolution of aerosol particles at UGR is driven by local emissions, mainly road traffic. During traffic rush hours, N_{CN} achieved its maximum values (19,900 cm^{-3} at 7:00 UTC and 18,300 cm^{-3} at 19:00 UTC). According to our results, CCN activity at UGR is clearly controlled by local emissions. Due to anthropogenic sources N_{CCN} can double its background value during the day (around 2000 cm^{-3} at $SS = 0.5\%$), achieving a maximum value of 4200 ± 3000 cm^{-3} at $SS = 0.5\%$ at 9:00 UTC. BC mass concentration showed two distinct maxima in coincidence with traffic rush hours. A decrease in AF and κ was observed during traffic rush hours, demonstrating the lower hygroscopicity and activation capacity of fresh traffic emissions.

At SNS, the mean value of N_{CCN} at $SS = 0.5\%$ was 820 ± 600 and N_{CN} was around 3000 ± 2800 cm^{-3} with $D_{geo} = 62$ nm. SNS exhibits higher AF values (AF is around 0.5 at $SS = 0.5\%$) than are found for UGR, and a more hygroscopic aerosol (the κ parameter is typically in the range from 0.1 to 0.3 at $SS = 0.50\%$). The diurnal evolution of BC mass concentrations at SNS exhibited a maximum around 12:00 UTC, associated with transport of pollutants from the urban area to Sierra Nevada due to the increase in the height of the ABL and upslope transport of pollutants. AF, κ and D_{geo} show a clear minimum around 14:00 UTC. At the same time, N_{CCN} at $SS = 0.5\%$ and N_{CN} exhibited their maximum values: 1300 ± 800 cm^{-3} and 6600 ± 4000 cm^{-3}. The observed diurnal cycles at SNS are attributed to the joint effect of ABL vertical transport of particles from Granada urban area to SNS and NPF during nucleation events in SNS. Clear differences were observed between non-event and NPF event days. The contribution of NPF to N_{CCN} at SNS was estimated to be 175% at $SS = 0.5\%$, suggesting NPF is the major CCN source at this site.

Different approaches were tested to estimate N_{CCN} from ancillary measurements at both sites. The high diversity in aerosol sources and processes affecting both environments could not be captured in one simple model. At UGR, characterized by high aerosol concentrations with high contribution of absorbing and non-hygroscopic aerosols such as BC, both models provided satisfactory results. In contrast, at SNS, which is characterized by low aerosol concentrations with low contribution of absorbing particles and large impact of NPF events, the new scheme proposed here based on N_{80} and D_{geo} provided better results, especially at high SS values. At low SS both models were unable to satisfactorily simulate the observations, probably due to the fact that the models are not able to reproduce the changes in aerosol properties during NPF events.

In summary, we demonstrated that CCN activity is driven by primary sources, mostly anthropogenic emissions, at an urban site while NPF events have a high impact on CCN concentration during summer time at a high mountain site. Moreover, this study highlights the need to consider these two mechanisms to develop a better CCN parameterization. This study points out the need to develop experimental campaigns to assess specific questions such as the role that the origin of NPF events (biogenic or anthropogenic, local or regional) may play in CCN concentrations, as well as long-term studies aiming to characterize CCN activation properties throughout the year, especially at SNS. Furthermore, additional measurements such as chemical composition and size-resolved measurements of CCN will allow a better understanding of the joined effects of ABL injections and NPF events and may help in identifying limitations of the simple models used here.

CRediT authorship contribution statement

Fernando Rejano: Conceptualization, Investigation, Methodology, Data curation, Writing - original draft, Visualization. **Gloria Titos:** Conceptualization, Investigation, Methodology, Writing - review & editing, Funding acquisition. **Juan Andrés Casquero-Vera:** Data curation, Formal analysis, Writing - review & editing. **Hassan Lyamani:** Conceptualization, Resources, Investigation, Writing - review & editing. **Elisabeth Andrews:** Writing - review & editing. **Patrick Sheridan:** Writing - review & editing. **Alberto Cazorla:** Supervision, Funding acquisition. **Sonia Castillo:** Visualization, Data curation. **Lucas Alados-Arboledas:** Writing - review & editing, Funding acquisition. **Francisco José Olmo:** Supervision, Project administration, Writing - review & editing, Funding acquisition.

Declaration of competing interest

The authors declare that they have no known competing financial interests or personal relationships that could have appeared to influence the work reported in this paper.

Acknowledgments

This work was supported by the European Union's Horizon 2020 research and innovation program through project ACTRIS-2 (grant agreement No 654109), by the Spanish Ministry of Science and Innovation through projects CGL2016-81092-R, CGL2017-90884REDT and RTI2018.101154.A.I00, by Junta de Andalucía, UGR and FEDER funds through project B-RNM-474-UGR18 and B-RNM-496-UGR18, by the Junta de Andalucía Excellence project P-18-RT-3820 and by University of Granada Plan Propio through Visiting Scholars program and Beca de Iniciación a la investigación en Máster. Gloria Titos is funded by Spanish Ministry of Science and Innovation under postdoctoral program Juan de la Cierva (IJCI-2016-29838). Juan Andrés Casquero-Vera is funded by MINECO under the predoctoral program FPI (BES-2017-080015).

Thanks to the NOAA Global Monitoring Laboratory for providing the data acquisition and processing system and for the use of the CCN counter.

Appendix A. Supplementary data

Supplementary data to this article can be found online at https://doi.org/10.1016/j.scitotenv.2020.143100.

References

Anderson, T.L., Ogren, J.A., 1998. Determining aerosol radiative properties using the TSI 3563 integrating nephelometer. Aerosol Sci. Technol. 29, 57–69. https://doi.org/10.1080/02786829808965551.

Andreae, M.O., Rosenfeld, D., 2008. Aerosol-cloud-precipitation interactions. Part 1. The nature and sources of cloud-active aerosols. Earth-Sci. Rev. 89, 13–41. https://doi.org/10.1016/j.earscirev.2008.03.001.

Andrews, E., Sheridan, P.J., Ogren, J.A., Hageman, D., Jefferson, A., Wendell, J., Alástuey, A., Alados-Arboledas, L., Bergin, M., Ealo, M., Sorribas, M., Sun, J., 2019. Overview of the NOAA/ESRL federated aerosol network. Bull. Am. Meteorol. Soc. 100, 123–135. https://doi.org/10.1175/BAMS-D-17-0175.1.

Asmi, E., Freney, E., Hervo, M., Picard, D., Rose, C., Colomb, A., Sellegri, K., 2012. Aerosol cloud activation in summer and winter at puy-de-Dôme high altitude site in France. Atmos. Chem. Phys. 12, 11589–11607. https://doi.org/10.5194/acp-12-11589-2012.

Bedoya-Velásquez, A.E., Navas-Guzmán, F., Granados-Muñoz, M.J., Titos, G., Román, R., Casquero-Vera, J.A., Ortiz-Amezcua, P., Benavent-Oltra, J.A., de Arruda Moreira, G., Montilla-Rosero, E., Hoyos, C.D., Artiñano, B., Coz, E., Olmo-Reyes, F.J., Alados-Arboledas, L., Guerrero-Rascado, J.L., 2018. Hygroscopic growth study in the framework of EARLINET during the SLOPE I campaign: synergy of remote sensing and in situ instrumentation. Atmos. Chem. Phys. 18, 7001–7017. https://doi.org/10.5194/acp-18-7001-2018.

Birmili, W., Ries, L., Sohmer, R., Anastou, A., Sonntag, A., König, K., Levin, I., 2009. Fine and ultrafine aerosol particles at the GAW station Schneefernerhaus/Zugspitze | Feine und ultrafeine aerosolpartikeln an der GAW-station Schneefernerhaus/Zugspitze. Gefahrstoffe Reinhaltung der Luft 69, 31–35.

Bougiatioti, A., Fountoukis, C., Kalivitis, N., Pandis, S.N., Nenes, A., Mihalopoulos, N., 2009. Cloud condensation nuclei measurements in the marine boundary layer of the eastern Mediterranean: CCN closure and droplet growth kinetics. Atmos. Chem. Phys. 9, 7053–7066. https://doi.org/10.5194/acp-9-7053-2009.

Bougiatioti, A., Nenes, A., Fountoukis, C., Kalivitis, N., Pandis, S.N., Mihalopoulos, N., 2011. Size-resolved CCN distributions and activation kinetics of aged continental and marine aerosol. Atmos. Chem. Phys. 11, 8791–8808. https://doi.org/10.5194/acp-11-8791-2011.

Bougiatioti, A., Bezantakos, S., Stavroulas, I., Kalivitis, N., Kokkalis, P., Biskos, G., Mihalopoulos, N., Papayannis, A., Nenes, A., 2016. Biomass-burning impact on CCN number, hygroscopicity and cloud formation during summertime in the eastern Mediterranean. Atmos. Chem. Phys. 16, 7389–7409. https://doi.org/10.5194/acp-16-7389-2016.

Kalkavouras, P., Bougiatioti, A., Kalivitis, N., Stavroulas, I., Tombrou, M., Nenes, A., Mihalopoulos, N., 2019. Regional new particle formation as modulators of cloud condensation nuclei and cloud droplet number in the eastern Mediterranean. Atmos. Chem. Phys. 19, 6185–6203. https://doi.org/10.5194/acp-19-6185-2019.

Burgos, M.A., Andrews, E., Titos, G., Alados-Arboledas, L., Baltensperger, U., Day, D., Jefferson, A., Kalivitis, N., Mihalopoulos, N., Sherman, J., Weingartner, E., Zieger, P., 2019. A global view on the effect of water uptake on aerosol particle light scattering. Sci. Data 6, 157. https://doi.org/10.1038/s41597-019-0158-7.

Burkart, J., Steiner, G., Reischl, G., Hitzenberger, R., 2011. Long-term study of cloud condensation nuclei (CCN) activation of the atmospheric aerosol in Vienna. Atmos. Environ. https://doi.org/10.1016/j.atmosenv.2011.07.022.

Casquero-Vera, J.A., Lyamani, H., Titos, G., Borrás, E., Olmo, F.J., Alados-Arboledas, L., 2019. Impact of primary NO<inf>2</inf> emissions at different urban sites exceeding the European NO<inf>2</inf> standard limit. Sci. Total Environ. 646, 1117–1125. https://doi.org/10.1016/j.scitotenv.2018.07.360.

Casquero-Vera, J.A., Lyamani, H., Dada, L., Hakala, S., Paasonen, P., Román, R., Fraile, R., Petäjä, T., Olmo-Reyes, F.J., Alados-Arboledas, L., 2020. New particle formation at urban and high-altitude remote sites in the south-eastern Iberian Peninsula. Atmos. Chem. Phys. Discuss. 2020, 1–32. https://doi.org/10.5194/acp-2020-394.

Che, H.C., Zhang, X.Y., Wang, Y.Q., Zhang, L., Shen, X.J., Zhang, Y.M., Ma, Q.L., Sun, J.Y., Zhang, Y.W., Wang, T.T., 2016. Characterization and parameterization of aerosol cloud condensation nuclei activation under different pollution conditions. Sci. Rep. 6. https://doi.org/10.1038/srep24497.

Che, H.C., Zhang, X.Y., Zhang, L., Wang, Y.Q., Zhang, Y.M., Shen, X.J., Ma, Q.L., Sun, J.Y., Zhong, J.T., 2017. Prediction of size-resolved number concentration of cloud condensation nuclei and long-term measurements of their activation characteristics. Sci. Rep. 7, 5819. https://doi.org/10.1038/s41598-017-05998-3.

Chen, L., Li, Q., Wu, D., Sun, H., Wei, Y., Ding, X., Chen, H., Cheng, T., Chen, J., 2019. Size distribution and chemical composition of primary particles emitted during open biomass burning processes: impacts on cloud condensation nuclei activation. Sci. Total Environ. 674, 179–188. https://doi.org/10.1016/j.scitotenv.2019.03.419.

Cheung, H.C., Chou, C.C.-K., Lee, C.S.L., Kuo, W.-C., Chang, S.-C., 2020. Hygroscopic properties and cloud condensation nuclei activity of atmospheric aerosols under the influences of Asian continental outflow and new particle formation at a coastal site in eastern Asia. Atmos. Chem. Phys. 20, 5911–5922. https://doi.org/10.5194/acp-20-5911-2020.

Collaud Coen, M., Weingartner, E., Nyeki, S., Cozic, J., Henning, S., Verheggen, B., Gehrig, R., Baltensperger, U., 2007. Long-term trend analysis of aerosol variables at the high-alpine site Jungfraujoch. J. Geophys. Res. Atmos. 112. https://doi.org/10.1029/2006JD007995.

Crosbie, E., Youn, J.-S., Balch, B., Wonaschütz, A., Shingler, T., Wang, Z., Conant, W.C., Betterton, E.A., Sorooshian, A., 2015. On the competition among aerosol number, size and composition in predicting CCN variability: a multi-annual field study in an urbanized desert. Atmos. Chem. Phys. 15, 6943–6958. https://doi.org/10.5194/acp-15-6943-2015.

Cubison, M.J., Ervens, B., Feingold, G., Docherty, K.S., Ulbrich, I.M., Shields, L., Prather, K., Hering, S., Jimenez, J.L., 2008. The influence of chemical composition and mixing state of Los Angeles urban aerosol on CCN number and cloud properties. Atmos. Chem. Phys. 8, 5649–5667. https://doi.org/10.5194/acp-8-5649-2008.

Dal Maso, M., Kulmala, M., Riipinen, I., Wagner, R., Hussein, T., Aalto, P.P., Lehtinen, K.E.J., 2005. Formation and growth of fresh atmospheric aerosols: eight years of aerosol size distribution data from SMEAR II, Hyytiälä, Finland. Boreal Environ. Res. 10, 323–336.

Dameto de España, C., Wonaschütz, A., Steiner, G., Rosati, B., Demattio, A., Schuh, H., Hitzenberger, R., 2017. Long-term quantitative field study of New Particle Formation (NPF) events as a source of Cloud Condensation Nuclei (CCN) in the urban background of Vienna. Atmos. Environ. 164, 289–298. https://doi.org/10.1016/j.atmosenv.2017.06.001.

De Arruda Moreira, G., Guerrero-Rascado, J.L., Benavent-Oltra, J.A., Ortiz-Amezcua, P., Román, R., Bedoya-Velásquez, A.E., Bravo-Aranda, J.A., Reyes, F.J.O., Landulfo, E., Alados-Arboledas, L., 2019. Analyzing the turbulent planetary boundary layer by remote sensing systems: the Doppler wind lidar, aerosol elastic lidar and microwave radiometer. Atmos. Chem. Phys. 19, 1263–1280. https://doi.org/10.5194/acp-19-1263-2019.

Després, V.R., Alex Huffman, J., Burrows, S.M., Hoose, C., Safatov, A.S., Buryak, G., Fröhlich-Nowoisky, J., Elbert, W., Andreae, M.O., Pöschl, U., Pöschl, U., Jaenicke, R., 2012. Primary biological aerosol particles in the atmosphere: a review. Tellus Ser. B Chem. Phys. Meteorol. 64. https://doi.org/10.3402/tellusb.v64i0.15598.

Duan, J., Wang, Y., Xie, X., Li, M., Tao, J., Wu, Y., Cheng, T., Zhang, R., Liu, Y., Li, X., He, Q., Gao, W., Wang, J., 2018. Influence of pollutants on activity of aerosol cloud condensation nuclei (CCN) during pollution and post-rain periods in Guangzhou, southern China. Sci. Total Environ. 642, 1008–1019. https://doi.org/10.1016/j.scitotenv.2018.06.053.

Ervens, B., Cubison, M.J., Andrews, E., Feingold, G., Ogren, J.A., Jimenez, J.L., Quinn, P.K., Bates, T.S., Wang, J., Zhang, Q., Flynn, M., Allan, J.D., 2010. CCN predictions using simplified assumptions of organic aerosol composition and mixing state: a synthesis from six different locations. Atmos. Chem. Phys. 10, 4795–4807. https://doi.org/10.5194/acp-10-4795-2010.

Fanourgakis, G.S., Kanakidou, M., Nenes, A., Bauer, S.E., Bergman, T., Carslaw, K.S., Grini, A., Hamilton, D.S., Johnson, J.S., Karydis, V.A., Wu, M., Yu, F., 2019. Evaluation of global simulations of aerosol particle and cloud condensation nuclei number, with implications for cloud droplet formation. Atmos. Chem. Phys. 19, 8591–8617. https://doi.org/10.5194/acp-19-8591-2019.

Gordon, H., Kirkby, J., Baltensperger, U., Bianchi, F., Breitenlechner, M., Curtius, J., Dias, A., Dommen, J., Donahue, N.M., Dunne, E.M., Yan, C., Carslaw, K.S., 2017. Causes and importance of new particle formation in the present-day and preindustrial atmospheres. J. Geophys. Res. Atmos. 122, 8739–8760. https://doi.org/10.1002/2017JD026844.

Gramsch, E., Muñoz, A., Langner, J., Morales, L., Soto, C., Pérez, P., Rubio, M.A., 2020. Black carbon transport between Santiago de Chile and glaciers in the Andes Mountains. Atmos. Environ. 232. https://doi.org/10.1016/j.atmosenv.2020.117546.

Gunthe, S.S., Rose, D., Su, H., Garland, R.M., Achtert, P., Nowak, A., Wiedensohler, A., Kuwata, M., Takegawa, N., Kondo, Y., Hu, M., Shao, M., Zhu, T., Andreae, M.O., Pöschl, U., 2011. Cloud condensation nuclei (CCN) from fresh and aged air pollution in the megacity region of Beijing. Atmos. Chem. Phys. 11, 11023–11039. https://doi.org/10.5194/acp-11-11023-2011.

Hammer, E., Gysel, M., Roberts, G.C., Elias, T., Hofer, J., Hoyle, C.R., Bukowiecki, N., Dupont, J.-C., Burnet, F., Baltensperger, U., Weingartner, E., 2014. Size-dependent particle activation properties in fog during the ParisFog 2012/13 field campaign. Atmos. Chem. Phys. 14, 10517–10533. https://doi.org/10.5194/acp-14-10517-2014.

Hegg, D.A., Radke, L.F., Hobbs, P.V., 1991. Measurements of Aitken nuclei and cloud condensation nuclei in the marine atmosphere and their relation to the DMS-cloud-climate hypothesis. J. Geophys. Res. 96. https://doi.org/10.1029/91jd01870.

Herenz, P., Wex, H., Mangold, A., Laffineur, Q., Gorodetskaya, I.V., Fleming, Z.L., Panagi, M., Stratmann, F., 2019. CCN measurements at the Princess Elisabeth Antarctica research station during three austral summers. Atmos. Chem. Phys. 19, 275–294. https://doi.org/10.5194/acp-19-275-2019.

Hirsikko, A., Bergman, T., Laakso, L., Dal Maso, M., Riipinen, I., Hõrrak, U., Kulmala, M., 2007. Identification and classification of the formation of intermediate ions measured in boreal forest. Atmos. Chem. Phys. 7, 201–210. https://doi.org/10.5194/acp-7-201-2007.

Intergovernmental Panel on Climate Change, 2014. Climate Change 2013 – The Physical Science Basis: Working Group I Contribution to the Fifth Assessment Report of the Intergovernmental Panel on Climate Change. Cambridge University Press, Cambridge https://doi.org/10.1017/CBO9781107415324.

Iwamoto, Y., Kinouchi, K., Watanabe, K., Yamazaki, N., Matsuki, A., 2016. Simultaneous measurement of CCN activity and chemical composition of fine-mode aerosols at Noto Peninsula, Japan, in Autumn 2012. Aerosol Air Qual. Res. 16, 2107–2118. https://doi.org/10.4209/aaqr.2015.09.0545.

Jefferson, A., 2010. Empirical estimates of CCN from aerosol optical properties at four remote sites. Atmos. Chem. Phys. 10, 6855–6861. https://doi.org/10.5194/acp-10-6855-2010.

Jurányi, Z., Gysel, M., Weingartner, E., Bukowiecki, N., Kammermann, L., Baltensperger, U., 2011. A 17 month climatology of the cloud condensation nuclei number concentration at the high alpine site Jungfraujoch. J. Geophys. Res. Atmos. 116. https://doi.org/10.1029/2010JD015199.

Jurányi, Z., Tritscher, T., Gysel, M., Laborde, M., Gomes, L., Roberts, G., Baltensperger, U., Weingartner, E., 2013. Hygroscopic mixing state of urban aerosol derived from size-resolved cloud condensation nuclei measurements during the MEGAPOLI campaign in Paris. Atmos. Chem. Phys. 13, 6431–6446. https://doi.org/10.5194/acp-13-6431-2013.

Kerminen, V.-M., Paramonov, M., Anttila, T., Riipinen, I., Fountoukis, C., Korhonen, H., Asmi, E., Laakso, L., Lihavainen, H., Swietlicki, E., Kulmala, M., Petäjä, T., 2012. Cloud condensation nuclei production associated with atmospheric nucleation: a synthesis based on existing literature and new results. Atmos. Chem. Phys. 12, 12037–12059. https://doi.org/10.5194/acp-12-12037-2012.

Kerminen, V.-M., Chen, X., Vakkari, V., Petäjä, T., Kulmala, M., Bianchi, F., 2018. Atmospheric new particle formation and growth: review of field observations. Environ. Res. Lett. 13, 103003. https://doi.org/10.1088/1748-9326/aadf3c.

Kim, J.H., Yum, S.S., Shim, S., Kim, W.J., Park, M., Kim, J.-H., Kim, M.-H., Yoon, S.-C., 2014. On the submicron aerosol distributions and CCN number concentrations in and around the Korean Peninsula. Atmos. Chem. Phys. 14, 8763–8779. https://doi.org/10.5194/acp-14-8763-2014.

Kim, N., Park, M., Yum, S.S., Park, J.S., Shin, H.J., Ahn, J.Y., 2018. Impact of urban aerosol properties on cloud condensation nuclei (CCN) activity during the KORUS-AQ field campaign. Atmos. Environ. 185, 221–236. https://doi.org/10.1016/j.atmosenv.2018.05.019 ISSN 1352-2310.

Köhler, H., 1936. The nucleus in and the growth of hygroscopic droplets. Trans. Faraday Soc. 32, 1152–1161. https://doi.org/10.1039/TF9363201152.

Laj, P., Bigi, A., Rose, C., Andrews, E., Lund Myhre, C., Collaud Coen, M., Wiedensohler, A., Schultz, M., Ogren, J.A., Fiebig, M., Gliß, J., Mortier, A., Pandolfi, M., Petäjä, T., Kim, S.-W., Aas, W., Putaud, J.-P., Mayol-Bracero, O., Keywood, M., Labrador, L., Aalto, P., Ahlberg, E., Alados Arboledas, L., Alastuey, A., Andrade, M., Art\'\iñano, B., Ausmeel, S., Arsov, T., Asmi, E., Backman, J., Baltensperger, U., Bastian, S., Bath, O., Beukes, J.P., Brem, B.T., Bukowiecki, N., Conil, S., Couret, C., Day, D., Dayantolis, W., Degorska, A., Dos Santos, S.M., Eleftheriadis, K., Fetfatzis, P., Favez, O., Flentje, H., Gini, M.I., Gregorič, A., Gysel-Beer, M., Hallar, G.A., Hand, J., Hoffer, A., Hueglin, C., Hooda, R.K., Hyvärinen, A., Kalapov, I., Kalivitis, N., Kasper-Giebl, A., Kim, J.E., Kouvarakis, G., Kranjc, I., Krejci, R., Kulmala, M., Labuschagne, C., Lee, H.-J., Lihavainen, H., Lin, N.-H., Löschau, G., Luoma, K., Marinoni, A., Meinhardt, F., Merkel, M., Metzger, J.-M., Mihalopoulos, N., Nguyen, N.A., Ondracek, J., Peréz, N., Perrone, M.R., Petit, J.-E., Picard, D., Pichon, J.-M., Pont, V., Prats, N., Prenni, A., Reisen, F., Romano, S., Sellegri, K., Sharma, S., Schauer, G., Sheridan, P., Sherman, J.P., Schütze, M., Schwerin, A., Sohmer, R., Sorribas, M., Steinbacher, M., Sun, J., Titos, G., Tokzko, B., Tuch, T., Tulet, P., Tunved, P., Vakkari, V., Velarde, F., Velasquez, P., Villani, P., Vratolis, S., Wang, S.-H., Weinhold, K., Weller, R., Yela, M., Yus-Diez, J., Zdimal, V., Zieger, P., Zikova, N., 2020. A global analysis of climate-relevant aerosol properties retrieved from the network of GAW near-surface observatories. Atmos. Meas. Tech. Discuss. 2020, 1–70. https://doi.org/10.5194/amt-2019-499.

Leng, C., Zhang, Q., Tao, J., Zhang, H., Zhang, D., Xu, C., Li, X., Kong, L., Cheng, T., Zhang, R., Wang, H., Chen, C., 2014. Impacts of new particle formation on aerosol Cloud Condensation Nuclei (CCN) activity in Shanghai: case study. Atmos. Chem. Phys. 14, 11353–11365. https://doi.org/10.5194/acp-14-11353-2014.

Lohmann, U., Feichter, J., 2005. Global indirect aerosol effects: a review. Atmos. Chem. Phys. 5, 715–737. https://doi.org/10.5194/acp-5-715-2005.

Lyamani, H., Olmo, F.J., Alados-Arboledas, L., 2005. Saharan dust outbreak over southeastern Spain as detected by sun photometer. Atmos. Environ. 39, 7276–7284. https://doi.org/10.1016/j.atmosenv.2005.09.011.

Lyamani, H., Olmo, F.J., Alados-Arboledas, L., 2008. Light scattering and absorption properties of aerosol particles in the urban environment of Granada, Spain. Atmos. Environ. 42, 2630–2642. https://doi.org/10.1016/j.atmosenv.2007.10.070.

Lyamani, H., Olmo, F.J., Alados-Arboledas, L., 2010. Physical and optical properties of aerosols over an urban location in Spain: seasonal and diurnal variability. Atmos. Chem. Phys. 10, 239–254. https://doi.org/10.5194/acp-10-239-2010.

Lyamani, H., Olmo, F.J., Foyo, I., Alados-Arboledas, L., 2011. Black carbon aerosols over an urban area in south-eastern Spain: changes detected after the 2008 economic crisis. Atmos. Environ. 45, 6423–6432. https://doi.org/10.1016/j.atmosenv.2011.07.063.

Lyamani, H., Fernández-Gálvez, J., Pérez-Ramírez, D., Valenzuela, A., Antón, M., Alados, I., Titos, G., Olmo, F.J., Alados-Arboledas, L., 2012. Aerosol properties over two urban sites in South Spain during an extended stagnation episode in winter season. Atmos. Environ. 62, 424–432. https://doi.org/10.1016/j.atmosenv.2012.08.050.

Meng, J.W., Yeung, M.C., Li, Y.J., Lee, B.Y.L., Chan, C.K., 2014. Size-resolved cloud condensation nuclei (CCN) activity and closure analysis at the HKUST Supersite in Hong Kong. Atmos. Chem. Phys. 14, 10267–10282. https://doi.org/10.5194/acp-14-10267-2014.

Merikanto, J., Spracklen, D.V., Mann, G.W., Pickering, S.J., Carslaw, K.S., 2009. Impact of nucleation on global CCN. Atmos. Chem. Phys. 9, 8601–8616. https://doi.org/10.5194/acp-9-8601-2009.

Moreira, G. de A., Guerrero-Rascado, J.L., Bravo-Aranda, J.A., Foyo-Moreno, I., Cazorla, A., Alados, I., Lyamani, H., Landulfo, E., Alados-Arboledas, L., 2020. Study of the planetary boundary layer height in an urban environment using a combination of microwave radiometer and ceilometer. Atmos. Res. 240, 104932. https://doi.org/10.1016/j.atmosres.2020.104932.

Motos, G., Schmale, J., Corbin, J.C., Zanatta, M., Baltensperger, U., Gysel-Beer, M., 2019. Droplet activation behaviour of atmospheric black carbon particles in fog as a function of their size and mixing state. Atmos. Chem. Phys. 19, 2183–2207. https://doi.org/10.5194/acp-19-2183-2019.

Müller, T., Henzing, J.S., de Leeuw, G., Wiedensohler, A., Alastuey, A., Angelov, H., Bizjak, M., Collaud Coen, M., Engström, J.E., Gruening, C., Hillamo, R., Hoffer, A., Imre, K., Ivanow, P., Jennings, G., Sun, J.Y., Kalivitis, N., Karlsson, H., Komppula, M., Laj, P., Li, S.-M., Lunder, C., Marinoni, A., Martins dos Santos, S., Moerman, M., Nowak, A., Ogren, J.A., Petzold, A., Pichon, J.M., Rodriquez, S., Sharma, S., Sheridan, P.J., Teinilä, K., Tuch, T., Viana, M., Virkkula, A., Weingartner, E., Wilhelm, R., Wang, Y.Q., 2011. Characterization and intercomparison of aerosol absorption photometers: result of two intercomparison workshops. Atmos. Meas. Tech. 4, 245–268. https://doi.org/10.5194/amt-4-245-2011.

O'Dowd, C.D., Hämeri, K., Mäkelä, J., Väkeva, M., Aalto, P., De Leeuw, G., Kunz, G.J., Becker, E., Hansson, H.-C., Allen, A.G., Jennings, S.G., Kulmala, M., 2002. Coastal new particle formation: environmental conditions and aerosol physicochemical characteristics during nucleation bursts. J. Geophys. Res. Atmos. 107. https://doi.org/10.1029/2000JD000206.

Paasonen, P., Peltola, M., Kontkanen, J., Junninen, H., Kerminen, V.M., Kulmala, M., 2018. Comprehensive analysis of particle growth rates from nucleation mode to cloud condensation nuclei in boreal forest. Atmos. Chem. Phys. 18. https://doi.org/10.5194/acp-18-12085-2018.

Pandolfi, M., Alados-Arboledas, L., Alastuey, A., Andrade, M., Angelov, C., Artiñano, B., Backman, J., Baltensperger, U., Bonasoni, P., Bukowiecki, N., Wiedensohler, A., Laj, P., 2018. A European aerosol phenomenology - 6: scattering properties of atmospheric aerosol particles from 28 ACTRIS sites. Atmos. Chem. Phys. 18, 7877–7911. https://doi.org/10.5194/acp-18-7877-2018.

Paramonov, M., Kerminen, V.-M., Gysel, M., Aalto, P.P., Andreae, M.O., Asmi, E., Baltensperger, U., Bougiatioti, A., Brus, D., Frank, G.P., Good, N., Gunthe, S.S., Hao, L., Irwin, M., Jaatinen, A., Jurányi, Z., King, S.M., Kortelainen, A., Kristensson, A., Lihavainen, H., Kulmala, M., Lohmann, U., Martin, S.T., McFiggans, G., Mihalopoulos, N., Nenes, A., O'Dowd, C.D., Ovadnevaite, J., Petäjä, T., Pöschl, U., Roberts, G.C., Rose, D., Svenningsson, B., Swietlicki, E., Weingartner, E., Whitehead, J., Wiedensohler, A., Wittbom, C., Sierau, B., 2015. A synthesis of cloud condensation nuclei counter (CCNC) measurements within the EUCAARI network. Atmos. Chem. Phys. 15, 12211–12229. https://doi.org/10.5194/acp-15-12211-2015.

Petters, M.D., Kreidenweis, S.M., 2007. A single parameter representation of hygroscopic growth and cloud condensation nucleus activity. Atmos. Chem. Phys. 7, 1961–1971. https://doi.org/10.5194/acp-7-1961-2007.

Petzold, A., Schönlinner, M., 2004. Multi-angle absorption photometry—a new method for the measurement of aerosol light absorption and atmospheric black carbon. J. Aerosol Sci. 35, 421–441. https://doi.org/10.1016/J.JAEROSCI.2003.09.005.

Pöhlker, M.L., Pöhlker, C., Ditas, F., Klimach, T., Hrabe de Angelis, I., Araújo, A., Brito, J., Carbone, S., Cheng, Y., Chi, X., Ditz, R., Gunthe, S.S., Kesselmeier, J., Könemann, T., Lavrič, J.V., Martin, S.T., Mikhailov, E., Moran-Zuloaga, D., Rose, D., Saturno, J., Su, H., Thalman, R., Walter, D., Wang, J., Wolff, S., Barbosa, H.M.J., Artaxo, P., Andreae, M.O., Pöschl, U., 2016. Long-term observations of cloud condensation nuclei in the Amazon rain forest – Part 1: Aerosol size distribution, hygroscopicity, and new model parametrizations for CCN prediction. Atmos. Chem. Phys. 16, 15709–15740. https://doi.org/10.5194/acp-16-15709-2016.

Reche, C., Querol, X., Alastuey, A., Viana, M., Pey, J., Moreno, T., Rodríguez, S., González, Y., Fernández-Camacho, R., De La Campa, A.M.S., Harrison, R.M., Quincey, P., 2011. New considerations for PM, black carbon and particle number concentration for air quality monitoring across different European cities. Atmos. Chem. Phys. 11, 6207–6227. https://doi.org/10.5194/acp-11-6207-2011.

Ren, J., Zhang, F., Wang, Y., Collins, D., Fan, X., Jin, X., Xu, W., Sun, Y., Cribb, M., Li, Z., 2018. Using different assumptions of aerosol mixing state and chemical composition to predict CCN concentrations based on field measurements in urban Beijing. Atmos. Chem. Phys. 18, 6907–6921. https://doi.org/10.5194/acp-18-6907-2018.

Ripoll, A., Minguillón, M.C., Pey, J., Jimenez, J.L., Day, D.A., Sosedova, Y., Canonaco, F., Prévôt, A.S.H., Querol, X., Alastuey, A., 2015. Long-term real-time chemical characterization of submicron aerosols at Montsec (southern Pyrenees, 1570 m a.s.l.). Atmos. Chem. Phys. 15, 2935–2951. https://doi.org/10.5194/acp-15-2935-2015.

Roberts, G.C., Nenes, A., 2005. A continuous-flow streamwise thermal-gradient CCN chamber for atmospheric measurements. Aerosol Sci. Technol. 39, 206–221. https://doi.org/10.1080/027868290913988.

Rose, D., Nowak, A., Achtert, P., Wiedensohler, A., Hu, M., Shao, M., Zhang, Y., Andreae, M.O., Pöschl, U., 2010. Cloud condensation nuclei in polluted air and biomass burning smoke near the mega-city Guangzhou, China – part 1: size-resolved measurements and implications for the modeling of aerosol particle hygroscopicity and CCN activity. Atmos. Chem. Phys. 10, 3365–3383. https://doi.org/10.5194/acp-10-3365-2010.

Rose, C., Sellegri, K., Moreno, I., Velarde, F., Ramonet, M., Weinhold, K., Krejci, R., Andrade, M., Wiedensohler, A., Ginot, P., Ginot, P., Laj, P., 2017. CCN production by new particle formation in the free troposphere. Atmos. Chem. Phys. 17, 1529–1541. https://doi.org/10.5194/acp-17-1529-2017.

Schmale, J., Henning, S., Decesari, S., Henzing, B., Keskinen, H., Sellegri, K., Ovadnevaite, J., Pöhlker, M., Brito, J., Bougiatioti, A., Baltensperger, U., Gysel, M., 2018. Long-term cloud condensation nuclei number concentration, particle number size distribution and chemical composition measurements at regionally representative observatories. Atmos. Chem. Phys. 18, 2853–2881. https://doi.org/10.5194/acp-18-2853-2018.

Seinfeld, J.H., Pandis, S.N., 1998. From air pollution to climate change. Atmos. Chem. Phys. 1326.

Seinfeld, J.H., Bretherton, C., Carslaw, K.S., Coe, H., DeMott, P.J., Dunlea, E.J., Feingold, G., Ghan, S., Guenther, A.B., Kahn, R., Kraucunas, I., Kreidenweis, S.M., Molina, M.J., Nenes, A., Penner, J.E., Prather, K.A., Ramanathan, V., Ramaswamy, V., Rasch, P.J., Ravishankara, A.R., Rosenfeld, D., Stephens, G., Wood, R., 2016. Improving our fundamental understanding of the role of aerosol-cloud interactions in the climate system.

Proc. Natl. Acad. Sci. U. S. A. 113, 5781–5790. https://doi.org/10.1073/pnas.1514043113.
Shen, Y., Virkkula, A., Ding, A., Luoma, K., Keskinen, H., Aalto, P.P., Chi, X., Qi, X., Nie, W., Huang, X., Petäjä, T., Kulmala, M., Kerminen, V.-M., 2019. Estimating CCN number concentrations using aerosol optical properties: role of particle number size distribution and parameterization. Atmos. Chem. Phys. Discuss., 1–40 https://doi.org/10.5194/acp-2019-149.
Titos, G., Jefferson, A., Sheridan, P.J., Andrews, E., Lyamani, H., Alados-Arboledas, L., Ogren, J.A., 2014a. Aerosol light-scattering enhancement due to water uptake during the TCAP campaign. Atmos. Chem. Phys. 14, 7031–7043. https://doi.org/10.5194/acp-14-7031-2014.
Titos, G., Lyamani, H., Pandolfi, M., Alastuey, A., Alados-Arboledas, L., 2014b. Identification of fine (PM1) and coarse (PM<10-1) sources of particulate matter in an urban environment. Atmos. Environ. 89, 593–602. https://doi.org/10.1016/j.atmosenv.2014.03.001.
Titos, G., del Águila, A., Cazorla, A., Lyamani, H., Casquero-Vera, J.A., Colombi, C., Cuccia, E., Gianelle, V., Močnik, G., Alastuey, A., Olmo, F.J., Alados-Arboledas, L., 2017. Spatial and temporal variability of carbonaceous aerosols: assessing the impact of biomass burning in the urban environment. Sci. Total Environ. 578, 613–625. https://doi.org/10.1016/j.scitotenv.2016.11.007.
Twomey, S., 1959. The nuclei of natural cloud formation part II: the supersaturation in natural clouds and the variation of cloud droplet concentration. Geofis. Pura Appl. 43, 243–249. https://doi.org/10.1007/BF01993560.
Valenzuela, A., Olmo, F.J., Lyamani, H., Antón, M., Quirantes, A., Alados-Arboledas, L., 2012. Aerosol radiative forcing during African desert dust events (2005–2010) over Southeastern Spain. Atmos. Chem. Phys. 12, 10331–10351. https://doi.org/10.5194/acp-12-10331-2012.
Venzac, H., Sellegri, K., Villani, P., Picard, D., Laj, P., 2009. Seasonal variation of aerosol size distributions in the free troposphere and residual layer at the puy de Dôme station, France. Atmos. Chem. Phys. 9, 1465–1478. https://doi.org/10.5194/acp-9-1465-2009.
Wang, J., Cubison, M.J., Aiken, A.C., Jimenez, J.L., Collins, D.R., 2010. The importance of aerosol mixing state and size-resolved composition on CCN concentration and the variation of the importance with atmospheric aging of aerosols. Atmos. Chem. Phys. 10, 7267–7283. https://doi.org/10.5194/acp-10-7267-2010.
Weger, M., Heinold, B., Engler, C., Schumann, U., Seifert, A., Fößig, R., Voigt, C., Baars, H., Blahak, U., Borrmann, S., Hoose, C., Kaufmann, S., Krämer, M., Seifert, P., Senf, F., Schneider, J., Tegen, I., 2018. The impact of mineral dust on cloud formation during the Saharan dust event in April 2014 over Europe. Atmos. Chem. Phys. 18, 17545–17572. https://doi.org/10.5194/acp-18-17545-2018.
Wiedensohler, A., Birmili, W., Nowak, A., Sonntag, A., Weinhold, K., Merkel, M., Wehner, B., Tuch, T., Pfeifer, S., Fiebig, M., Fjäraa, A.M., Asmi, E., Sellegri, K., Depuy, R., Venzac, H., Villani, P., Laj, P., Aalto, P., Ogren, J.A., Swietlicki, E., Williams, P., Roldin, P., Quincey, P., Hüglin, C., Fierz-Schmidhauser, R., Gysel, M., Weingartner, E., Riccobono, F., Santos, S., Grüning, C., Faloon, K., Beddows, D., Harrison, R., Monahan, C., Jennings, S.G., O'Dowd, C.D., Marinoni, A., Horn, H.-G., Keck, L., Jiang, J., Scheckman, J., McMurry, P.H., Deng, Z., Zhao, C.S., Moerman, M., Henzing, B., de Leeuw, G., Löschau, G., Bastian, S., 2012. Mobility particle size spectrometers: harmonization of technical standards and data structure to facilitate high quality long-term observations of atmospheric particle number size distributions. Atmos. Meas. Tech. 5, 657–685. https://doi.org/10.5194/amt-5-657-2012.
Wu, Z.J., Poulain, L., Birmili, W., Größ, J., Niedermeier, N., Wang, Z.B., Herrmann, H., Wiedensohler, A., 2015. Some insights into the condensing vapors driving new particle growth to CCN sizes on the basis of hygroscopicity measurements. Atmos. Chem. Phys. 15, 13071–13083. https://doi.org/10.5194/acp-15-13071-2015.
Wu, Z., Zheng, J., Wang, Y., Shang, D., Du, Z., Zhang, Y., Hu, M., 2017. Chemical and physical properties of biomass burning aerosols and their CCN activity: a case study in Beijing, China. Sci. Total Environ. 579, 1260–1268. https://doi.org/10.1016/j.scitotenv.2016.11.112.
Yli-Juuti, T., Riipinen, N., Aalto, P.P., Nieminen, T., Maenhaut, W., Janssens, I.A., Claeys, M., Salma, I., Ocskay, R., Hoffer, A., Lmre, K., Kulmala, M., 2009. Characteristics of new particle formation events and cluster ions at K-puszta, Hungary. Boreal Environ. Res. 14, 683–698.
Zeb, B., Alam, K., Nasir, J., Mansha, M., Ahmad, I., Bibi, S., Malik, S.M., Ali, M., 2020. Black carbon aerosol characteristics and radiative forcing over the high altitude glacier region of Himalaya-Karakorum-Hindukush. Atmos. Environ. 238. https://doi.org/10.1016/j.atmosenv.2020.117711.
Zhang, F., Wang, Y., Peng, J., Ren, J., Collins, D., Zhang, R., Sun, Y., Yang, X., Li, Z., 2017. Uncertainty in predicting CCN activity of aged and primary aerosols. J. Geophys. Res. Atmos. 122, 11,711–723,736. https://doi.org/10.1002/2017JD027058.
Zhang, Y., Tao, J., Ma, N., Kuang, Y., Wang, Z., Cheng, P., Xu, W., Yang, W., Zhang, S., Xiong, C., Dong, W., Xie, L., Sun, Y., Fu, P., Zhou, G., Cheng, Y., Su, H., 2020. Predicting cloud condensation nuclei number concentration based on conventional measurements of aerosol properties in the North China Plain. Sci. Total Environ. 719, 137473. https://doi.org/10.1016/j.scitotenv.2020.137473.